PHOTOCATALYTIC DEGRADATION OF PERSISTENT ORGANIC POLLUTANTS FROM WATER USING NANOSTRUCTURED METAL OXIDES

BY

MOHAMMED ALTAHIR IBRAHIM SULIMAN

A Thesis Presented to the
DEANSHIP OF GRADUATE STUDIES

KING FAHD UNIVERSITY OF PETROLEUM & MINERALS

DHAHRAN, SAUDI ARABIA

In Partial Fulfillment of the
Requirements for the Degree of

MASTER OF SCIENCE

In

CHEMISTRY

MAY, 2017

KING FAHD UNIVERSITY OF PETROLEUM & MINERALS

DHAHRAN- 31261, SAUDI ARABIA

DEANSHIP OF GRADUATE STUDIES

This thesis, was written by **MOHAMMED ALTAHIR IBRAHIM SULIAMN** under the direction of his thesis advisor and approved by his thesis committee, has been presented and accepted by the Dean of Graduate Studies, in partial fulfillment of the requirements for the degree of **MASTER OF SCIENCE IN CHEMISTRY.**

Dr. Basheer Chanbasha
(Advisor)

6/6/2017

Dr. Abdulaziz Al-Saadi
Department Chairman

Prof. Mohammed Ashraf Gondal
(Member)

Dr. Sulayman A. Oladepo
(Member)

Dr. Salam A. Zummo
Dean of Graduate Studies

7/6/17

Date

Dedication

To my parents, especially my mam Lila may Allah give her happiness, health, and heaven in the afterlife. For my Brother, Moaz and my two lovely sisters Arwa and Razan for their continuous support through the years.

ACKNOWLEDGMENTS

I would like to start by thanking Allah, lord of all worlds, for everything. I would like to express my deepest gratitude to an academic advisor, Dr. Basheer Chanbasha, for his worthy advice, assistance, and guidance through my research years. I would also like to extend my sincere thanks to my committee members, Prof. Mohammed Ashraf Gonadal and Dr. Sulayman Oladepo, for their professional suggestions and review of my dissertation.

I especially wish to thank National University of Singapore (NUS) for their kind accommodation, fruitful collaboration work and using all the facilities as well as pursuing research in Chemistry Department. Special thanks to Dr. Chuah Gaik Khuan for under her supervising during my research in NUS.

I cannot express the depth of my gratitude in words to mother and father, for all the love and their prayer for me all the time since when I was just kids and sacrifice for me. I also give thanks to my brother and my lovely sisters for support and persistent interest. Special acknowledgment must be given to the staff and faculty member at Chemistry department for their support. Special appreciations are forwarded to the chairman Dr. Abdulaziz Al-Saadi for continuous support and encouragements

TABLE OF CONTENTS

LIST OF TABLES

LIST OF FIGURES

LIST OF ABBREVIATIONS

A : Acceptor

AOPs : Advanced oxidation processes

ASAP : A micrometrics accelerated surface area and porosimeter (ASAP)

Aps : Alkyl phenol

BET : Brunauer-Emmett-Teller

BJH : Barrett-Joyner-Halanda

BQ : 1,4-benzoquinone

C_0 : Initial concentration of pollutant

C : Concentration of the pollutant at time t

CTAB : Cetyltrimethylammonium bromide

cb : Conduction band

e_{cb}^- : Conduction band electron

D : Donor

E_g : Band gap energy

eV : Electron volts

EDX : Energy dispersive x- ray Spectroscopy

HRTEM : High-resolution transmission electron microscopy

h_{vb}^{+} : Valance band hole

h^{+} : hole

HPLC : High performance liguid chromatography

K.M : Kubelka–Munk

IUPAC : International Union of Pure and Applied Chemistry

JCPDS : Joint Committee on Powder Diffraction Standards

LC-MS : Liquid chromatography mass spectroscopy

mg/l : milligram per liter

MTBE : Methyl tert-butyl ether

m-WO_3 : mesoporous WO_3

M : mole/l

NP : Nanoparticle (s)

$O_2^{\bullet-}$: Super oxide radical

$^{\bullet}OH$: Hydroxide radical (s)

PCBs : Polychlorinated biphenyls

ppm : parts per million

SBA : Santa Barbara Amorphous type material

SEM : Scanning electron microscopy

SC : Semiconductor

SPR : Surface plasmatic resonance

TEM : Transmission electron microscopy

TEOS : Tetraethyl orthosilicate

DRS : Diffuse Reflectance Spectroscopy

UV : Ultraviolet

UV-Vis : UV-Visible

Vb : Valence band

XPS : X-ray Photoelectron Spectroscopy

XRD : X-ray diffraction

λ : wavelength of light

θ : diffraction angle

°C : degree Celsius

ABSTRACT

Full Name : Mohammed Altahir Ibrahim Suliman

Thesis Title : Photocatalytic degradation of persistent organic pollutants from water using nanostructured metal oxides

Major Field : Chemistry

Date of Degree : May, 2017

In the presented work, photocatalytic method was developed for the degradation of Atrazine in water samples. Highly ordered mesoporous Ag-WO_3/SBA-15 composites were tested as photocatalysts for the degradation of atrazine in water. It was found that 40 % WO_3 loading rendered an optimum surface area and material content in the SBA-15 template and hence favored the enhanced photocatalytic degradation of atrazine. The further addition of Ag nanoparticle onto the WO_3/SBA-15 composite not only made this catalyst very effective in the most sought visible region due to solar energy harvesting, but also significantly reduced the electron-hole recombination as evidenced by photoluminescence studies to enhance the degradation efficiency. As a result, the Ag-WO_3/SBA-15 composite the photocatalytic degradation of atrazine in water under visible radiation was significantly enhanced.

Furthermore, series of novel photocatalysts were synthesized and a significant enhancement photocatalytic degradation of atrazine and methylparaben in water was achieved under visible light excitation, when the Ag nanoparticles (NPs) loaded AgBr-mesoporous-WO_3 composite was used. The enhanced photocatalytic degradation is due to the surface plasmonic resonance (SPR) resulted from the introduction of Ag nanoparticles (NPs) on the surface of the catalyst, besides the reduction of electron-hole

recombination brought about by the formation of heterojunction in the semiconductor composite. Highly ordered mesoporous-WO_3 (m-WO_3) was synthesized by sol-gel method and AgBr (NPs) were introduced in the pores of m-WO_3 and subsequently, Ag nanoparticles were introduced by light irradiation. The morphological and optical characterization of the synthesized photocatalysts was carried out using SEM, TEM, XDR, N_2 adsorption-desorption, UV-Vis diffuse reflectance spectroscopy (DRS). Also, the photocatalytic studies using radical scavengers indicated that $O_2^{-\bullet}$, $^{\bullet}OH$, and Br^0 are the main reactive species.

ABSTRACT IN ARABIC

الاسم الكامل: مُحمّد الطَّاهر إبراهيم سُليمان

عنوان الرسالة: التحفيز الضوئي لتكسير الملوثات العضوية من المياه باستخدام أكاسيد المعادن النانوية

التخصص: كيمياء

تاريخ الدرجة العلمية: ابريل 2017

في هذا العمل لقد قمنا بتحضير عدد من المحفزات الضوئية من مركبات اكاسيد الفلز النانوية وتم دراسة تاثير هذه المحفزات في تكسير الملوثات العضوية صعبة الإزاله في عينات من الماء. اجريت التجارب علي مركبات عالية الترتيب المثقبه من مركبات (مركبات الفضة / ثالث اوكسيد التنجستن) لتكسير مركب الاترازين في الماء. وجد ان اربعين بالمئة من ثالث اوكسيد التنجستن المطلي بمادة (SBA-15) وذات مساحة السطح العالية هوالمحفز الانسب لتكسير مركب الاترازين في الماء. بالاضافة الى ذلك، وجد ان إضافة عنصر الفضة على سطح معقد ثالث اكسيد التنجستن/(SBA-15) ليس فقط انه يستخدم اشعة الضوء المرئي بل تعدى الى انه يمكن ان يقلل من انكماش الالكترون والكيان الموجب والذي اثبت عن طرق دراسة التوهج. ونتيجة لذلك وجد ان المعقد فعال جدا لتكسير مركب الاترازين تحت اشعة الضوء المرئ.

وبالاضافة الى ما ذكر اعلاه تم تحضير عدد من المعقدات التحفيز الضوئي من ($Ag/AgBr@m\text{-}WO_3$) حيث وجد انها قادرة على تكسير مركب المثيل برابين حيث وجد انه عندما اضيف عنصر الفضة النانوي على سطح بروميد الفضد الموجود على سطح ثالث اكسيد التنجستن المنفذ. قد تبين ان هناك زيادة في كفاءة تكسير الميثيل برابين وذلك نسبة لظاهرة بلازمن السطوح الناتج من وجود ذرات الفضة نانوية الحجم على سطح المحفز اضافة الى ان تقليل انكمشاش الالكترون مع الكيان الموجب والذي نشأه بدوه عن طرق التكوين المتغاير بين معقد شبة الموصل. تم تحضير معقد ثالث اوكسيد التنجستن شبه المنفذ بواسطة طريقة الصول جل ومن ثم تم اضافة جزيئات بروميد الفضة على ثقوب ثالث اكسيد التنجستن المثقب. ثم تلا ذلك اضافة جزيئات الفضة النانوية على سطح المعقد عن طريق الاختزال الضوئي. لقد تم اجراء كل عمليات الوصف الضوئي والشكلي لمركبات المحفز الضوئي ومن ثم الكشف عن مقعد المحفز الضوئي التصوير بواسطة المجهر الالكتروني وناقل المجهر الالكتروني وحيود مسحوق الاشعة السينية

والامتزاز الامتصاص للنتروجين والاشعة فوق البنفسجية منتشر الانعكاس وتم دراسة كل ما ذكر سابقا للمحفز الحضر، واخير تمت دراسة الشقوق الحرة المشطة النشطة والمسئولة عن التكسير حيث وجود ان شق حر الهيدروكسيل ووشق حر ايون الاكسجين وذرة البروم هم الجزئيات النشطة والمسئولة عن تكسير مثيل برابين.

CHAPTER 1

INTRODUCTION

1.1 Introduction

Even though water is abundant on Earth, covering 72% of the earth's surface, however, 0.5% of it is freshwater, and of this, less than 1% is readily accessible for human use[1]. Unfortunately, pollution of water becomes a prevalent threat with the fast development of human societies. Organic pollutants are being produced and applied in large amounts worldwide and in the kingdom, due to petrochemical, paint, leather and textile industries. Widespread contamination of water by organic matter has been recognized as an issue of great concern.

1.2 Examples of common pollutants in water

Several sources of water pollutants can contaminate our ecosystem.

(i) Industrial products (lubricants, additive and flame retardants):

Polychlorinated biphenyls (PCBs), polybrominated and diphenylethers.

(ii) Industrial product (petrochemicals, solvents, intermediates):

For example, water contaminated with various organic species (like Methyl-t-butylether, BTEX (benzene, xylene, toluene), dyes, acetaldehyde,

alkylphenols, Methyl tert-butyl ether (MTBE) is a carcinogen to humans and is of considerable health concern, even at low (ppm) concentrations.

(iii) Biocide (nonagricultural biocides, pesticides): dichlorodiphenyltrichloroethane, tributyltin, triclosan and atrazine.

(iv) Consumer products (pharmaceuticals, detergents, personal care products):

Firstly, surfactant, synthetic fragrances in which surfactant such as alkyl phenol (APs), alkyl. alkyl phenol carboxylate and phenol ethoxylates (APEOs). Secondly parabens (e.g. methyl, ethyl propyl- and butylparaben) as an example of preservatives.

(v) Disinfection by-products: such as dichloromethane, haloacetic acids, and bromate.

(vi) Natural chemical / geogenic (heavy metals, inorganic, cyanotoxines, odor, and taste):

Mercury, arsenic, lead, selenium, fluoride, uranium, geosmin, methylisobornel, estrodiol.

(vii) Transformation products (metabolites from above chemicals):

Chloroacetanilide herbicide metabolites and metaboliteis of perfluorinated compounds.

The efficient reduction/removal of these organic compounds from water is highly desirable for waste water treatment to fulfill the future needs of any country by reuse of water. Many methods have been developed for removal of organic species but still, the quest for efficient and cost-effective removal of organic matter in waste water is at full swing. The conventional setups for photocatalysis are based on broad spectral lamps and which are not effective in terms of reaction rate and requires longer exposure time. For

efficient photocatalytic removal of organic pollutants and to overcome the main challenges such as longer exposure time, high reaction rate, in photocatalytic process being currently applied in conventional ready-made setups, we shall design special reactor and apply unique source of radiation like UV/ Visible or lasers to enhance the reaction rate and efficient removal of dyes or persistent organic pollutant in waste water initially. Once the best catalyst and an excitation wavelength of the laser is identified through laboratory scale experiments, a solar-based prototype system will be designed for field applications.

Approximately one billion of people in urban area have no access to a clean source of drinking water especially in Asia, Africa and the Caribbean and Latin America. The effects of polluted water on the health of more than 1.2 billion people was estimated and every year contributes to the death of 15 million children due to water-borne diseases[1]. Due to these causes, the need for development of specific disinfection techniques to achieve the objective of water treatment and making better water quality in terms of reliability, in addition to economic and environmental criteria[2]. Various chemical processes like chlorination activated carbon, multimedia sand filtration and coagulation have been applied for removing microorganisms[3–7]. However, further perfections of this process are required to enhance the efficiency of the photocatalytic process for purification of water.

1.3 Statement of Problem

Effective removal of toxic organic substances from water can provide a substantial contribution to its water treatment, which ensures sustainability. Moreover, the recovery

of organic contaminated and polluted waters (or reutilized in a closed system) results into vital savings of water resources.

In addition, considering the stability, toxicity, and carcinogenicity, organic pollutants have caused considerable damage to the ecosystem, human and aquatic lives. Hence, an environmentally friendly and relatively cheap advanced technology must be developed to degrade these pollutants.

Titanium oxide under irradiation by ultraviolet rays of natural or artificial lighting has been found effective in photocatalytic technology. Besides been a cheap and readily available material with high oxidizing power; and in addition to fulfilling the above qualities of a good photocatalyst, TiO_2 does not require constant feeding as it is not used up in a pollutant degradation process; it acts for a very long time while been effective, stable and non-toxic. The disadvantage of the large band gap of 3.2 eV and UV irradiation timing is a major factor affecting TiO_2/UV light process. Roughly 4% of the solar flux present in the atmosphere contains UV radiation beneficial for photocatalysis; although high energy UV radiation needed, has a wavelength range that is not available to the earth. Therefore, the UV radiation in the solar flux is not of the appropriate and needed wavelength required to carry out photocatalysis; which makes it more expensive to use the natural source. This in turn limits the photocatalytic application of TiO_2 to UV range of the spectrum.

Therefore, improving the optical properties of TiO_2 by modifying its band gap is necessary, so the development of new materials is needed to increase the photocatalytic activity for the practical applications using visible/solar energyThus, to have high

efficiency and ability for utilizing solar power, semiconductors must have the following requirement:

(i) non-toxicity, (ii) large surface area, (iii) broad absorption spectra with high absorption coefficients, (iv) displaying tunable properties which can be modified by size reduction, doping, photosensitizers, etc., (v) possessing facility for multielectron transfer process and (vi) high photocatalytic activity stability. Thus, metal oxides will be synthesized, investigated and doped with metals with appropriate properties depending on the photodegradation application.

1.4 Objectives of the study

The major objective of this work is to study the photocatalytic activity of novel nanomaterials for environmental applications. The specific objectives can be subdivided as follows:

- Synthesis of different catalysts (modified WO_3, metal doped WO_3, and another metal oxide doped and un-doped) using hydrothermal method.
- Characterization and morphological studies of synthesized catalysts using X-ray Diffraction (XRD), Scanning Electron Microscopy (SEM) and Transmission Electron Microscopy (TEM).
- Development of an experimental setup for UV visible light photocatalytic process for degradation of organic pollutants such as hazardous disinfection by-product and pharmaceutical compounds from water.

- Identification of products by some chromatographic technique such as high performance liquid chromatography (HPLC) and (Liquid chromatography mass spectroscopy (LC-MS).

CHAPTER 2

LITERATURE REVIEW

2.1 Photocatalysis

Photocatalysis is a term used to a process in which light changes the rate of chemical reaction in the presence of a catalyst that absorbs the light. This light absorbing catalyst is referred to as the photocatalyst. Initial concern in the study of photocatalysis started when Fujishima and Honda studied photocatalytic splitting of water into oxygen and hydrogen using TiO_2 in 1970[8]. Photocatalytic reactions may occur either homogeneously or heterogeneously. The most common materials used in heterogeneous photocatalysis are semiconductors having unique properties. Moreover, their high stability facilitated by solid form and mobility of charge for interaction with adsorbate molecule in the surrounding medium[9,10].

2.2 Heterogeneous photocatalytic reactions

The heterogeneous process occurs in binary phase system (solid-gas or solid-liquid) in which a semiconductor is usually used as a photocatalyst. In this case, the formation of active sites initiated by the absorption of light on the photocatalyst surface i.e. electron-hole pairs, that interact with substrate absorbed on its surface[11].

On the other hand, homogeneous processes are single phase systems (liquid), in which the absorption of a photon is carried out by the catalyst species, such as an organic dye,

an ion salt solution[12], or a transition metal complex[13,14]. In homogeneous photocatalysis, the reaction is accelerated by the excited state of the catalyst, which is generated as a result of radiation absorption. Furthermore, their solid form facilitates high stability and mobility of charge for interaction with the adsorbate molecules in the surrounding medium.

In the photocatalytic process, a semiconductor catalyst absorbs an ultraviolet photon and produces powerful oxide ($O_2^{\bullet-}$) and hydroxide radicals ($^{\bullet}OH$) in an aqueous solution[15–19]. When the semiconductor absorbs UV laser light, an electron is transferred from the valence band to conduction band. By this process, an electron/hole pair is produced. The surfaces of the catalyst become an oxidizing and reducing agent when the electron (e^-) and hole (h^+) are separated relocated to the surface of the catalyst. In aqueous solution, these two surfaces produce hydroxide ($^{\bullet}OH$) and oxide radicals ($O_2^{\bullet-}$). These free radicals have the ability to decompose many organic substances such as benzene, formaldehyde, and bacteria, in addition to some inorganic contaminations such as ammonia into harm-free substances like H_2O and CO_2.

This photocatalytic process is effective for both cleaning water and air. The catalysts activate moisture and oxygen in air and produce free radicals ($O_2^{\bullet-}$) and ($^{\bullet}OH$) which can transform harmful air and organic substances into H_2O and CO_2. It has more powerful oxidation ability than ozone and negative oxygen ion.

Moreover, some photocatalyst has the great hydrophobic capacity and retains contamination, and can preserve new buildings clean for a long time. Most of these catalysts are inert and non-toxic. The improvement in the rate of reaction is one of the

most demanding tasks in photocatalysis. It should be noteworthy to mention that all previous work focuses on broad spectral radiation sources such as a lamp and TiO_2 when treating bacteria disinfection from waste water using heterogeneous photocatalysis[20–24].

Use of lamps emitting over a broad spectral wavelength range is associated with several problems. For instance, the presence of power instability during operation due to overheating of lamps. In addition, there is low delivery of photons, low photonic efficiency of photons to the reaction zone. One of the major drawbacks associated with UV lamps as a source of irradiation is longer exposure times for complete removal of pollutants.

One of the characteristic features of semiconductor (SC) is an electronic band structure in which the highest occupied energy band was known as the valence band (vb) and conduction band is a lowest unoccupied empty band (cb) which are separated by an energy gap known as band gap (E_g). This band gap is the region of forbidden energies in a perfect crystal. The semiconductor particle is absorbed an energy when an incident photon of energy equal or greater than the band gap as result of this an electron (e_{cb}^-) from the (vb) is promoted to the conduction band with a simultaneous generation of a positive entity in the valance band a "hole" (h_{vb}^+). The e_{cb}^- and h_{vb}^+ can be held on the surface in the bulk of the particle in a few nanoseconds by dissipating energy as heat or can be trapped in the surface states where they can react with the donor (D) or acceptor (A) species adsorbed or close to the surface of the particle. Thereby, it will initiate anodic and cathodic reactions[10,25–30] as shown in Fig. 2.1.

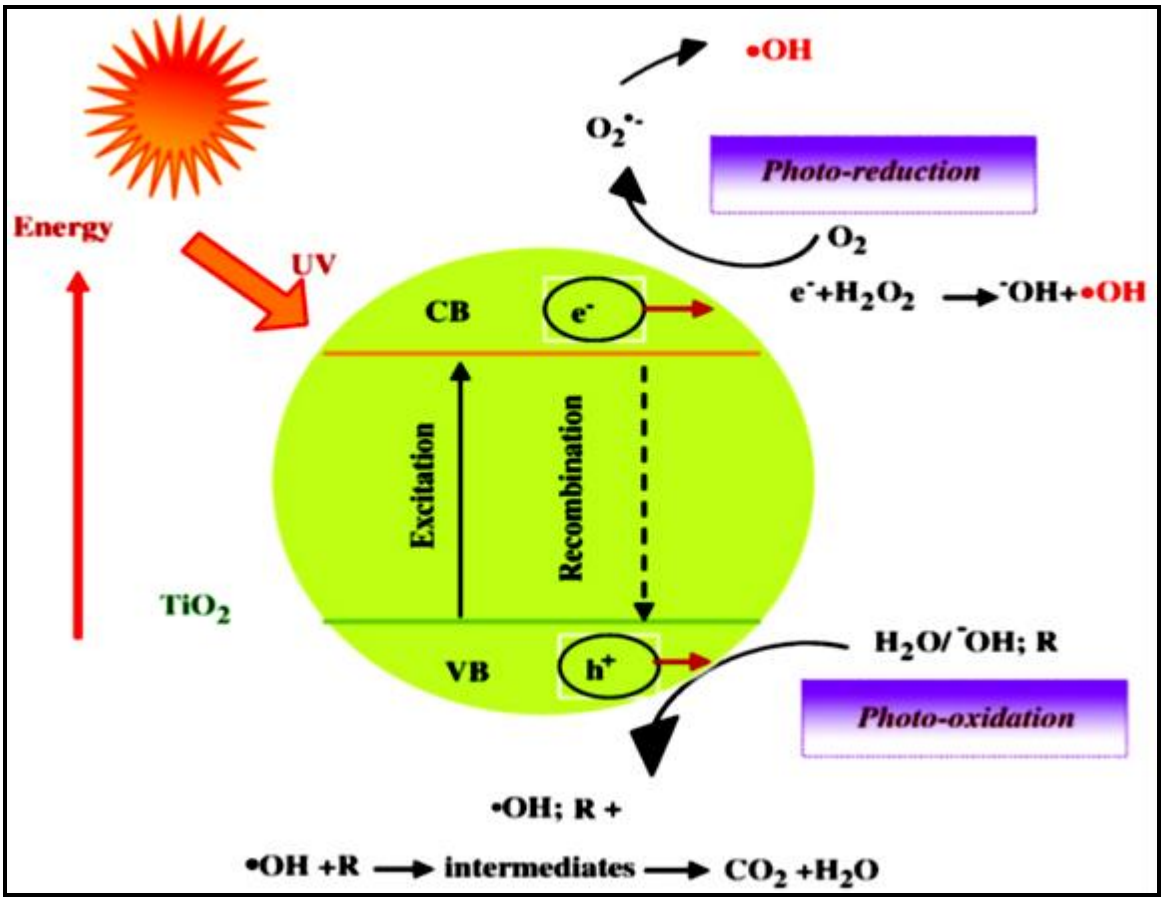

Figure 2.1: Schematic representation of redox reaction at the surface of a photocatalyst

2.2.1 General Mechanism of heterogeneous photocatalysis

In principle, a photocatalytic reaction proceeds on the surface of the semiconductor via many steps. Fig. 2.2 illustrates a reaction process detailed of the generating electron-hole pairs and the corresponding redox reaction take place on the semiconductor surface when irradiated with an appropriate wavelength of light. Heterogeneous photocatalysis is a complex sequence of the reactions. Its mechanism composes of five steps[31], which are:

(a) Mass transfer of the organic contaminant in the liquid phase to the TiO_2 surface.

(b) Adsorption of the organic contaminant onto the photon activated TiO_2 surface.

(c) Photocatalysis reaction for the adsorbed phase on the TiO_2 surface.

(d) Desorption of the intermediate from the TiO_2 surface.

(e) Mass transfer of the intermediate from the interface region to the bulk fluid.

The main difference of classic heterogeneous catalysis with photocatalysis is the initiation of the chemical transformation during step (c), in which the photoexcitation is the case of photocatalysis instead of the thermal activation of classic catalysis.

The photocatalytic reaction in step (c) is a complex surface process that starts with the absorption of a photon with energy (E) equal or higher than the energy bandgap (E_g) of the photocatalyst (WO_3). The initiating step of the photocatalytic process is the absorption of the photon which leads to charge carrier generation: the photoexcited electron e_{cb}^- and the hole h_{vb}^+.

$$WO_3 + h_{vb}^+ \rightarrow h^+ + e_{cb}^- \qquad (2.1)$$

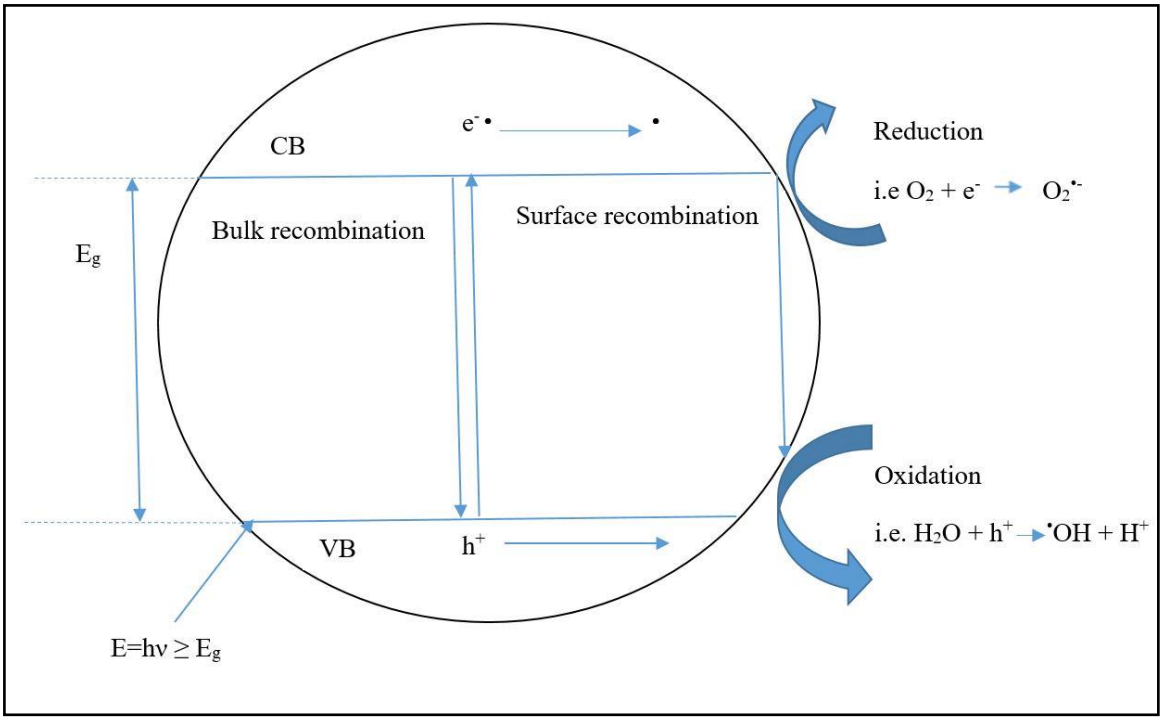

Figure 2.2: Mechanism scheme for photocatalysis.

In the presence of surface charge region, when the semiconductor is in contact with liquid, the electron-hole pair can be separated and migrated to the surface due to the potential gradient between bulk solid and its external surface.

During the transport of electron and hole to the catalyst surface, they can also recombine and generate heat (Eq. 2.2) and this recombination process results in the low quantum efficiencies for the photocatalytic process. Alfano et al[32] reported that the recombination of electron and hole occur mainly in the bulk of the catalyst particles. This recombination process can be reduced greatly if these mobile species are separated and subsequently, trapped by defects, surface adsorbates or other sites.

$$h_{vb}^{+} + e_{cb} \rightarrow heat \qquad bulk\ recombination \quad (2.2)$$

2.3 Water treatment method

Various kinds of water treatment methods have been used, part of which have been commercially applied in water treatment plants. The classification of these methods can be divided into four categories: chemical methods, physical methods, a combination of chemical and physical methods and biological methods.

However, most of the commonly used technologies for water treatment suffer from different limitations. For example, most chemical, physical and combined methods are expensive and may produce a toxic secondary pollutants to the ecosystem, meanwhile intensive usage of chemicals such as chlorine, ammonia, hydrochloric acid, ozone, permanganate, ion exchange resin, sodium hydroxide, etc.) are introduced while the treatment process so that residuals resulting from the treatments (toxic waste, brine, sludge, etc.) are persisted in treatment water source[33]. Furthermore, the physical methods such as coagulation or adsorption can only transfer the pollutant from one phase to another rather than completely "elimination" or "deserting" the pollutants[34]. Regarding the biological methods, although they are showed to be effective to several sorts of contaminants, the drawbacks are clearly revealed in form of waste sludge disposal, volatile emissions, high energy costs, temperature sensitivity and relatively long period of treatment time[35,36]. Thus, it critical considering the importance of developing more beneficial wastewater treatment methods.

CHAPTER 3

Analytical Techniques

3.1 Introduction

The physical and chemical properties of semiconductor photocatalyst such crystalline phase, particle size, crystal, surface area and porosity and surface composition strongly influence its effectiveness as a photocatalyst. In this manner, the accurate of characterization of material's properties is the critical point for the assessment of photocatalyst synthesis techniques and elucidation of photoactivity results.

In this chapter, the concept and basic principles concerning the analytical techniques used in this work for the characterization of WO_3 photocatalyst and their composites are briefly discussed.

3.2 X-Ray Diffraction (XRD)

XRD is a powerful, nondestructive technique, reliable and quick technique for the determination of crystallographic properties of solid materials. XRD technique takes advantages on the coherent scattering of X-rays by crystalline and polycrystalline solids to obtain a diffraction pattern, which is unique and can be considered as a fingerprint of the materials itself. The crystalline materials are consisting of lattice planes, and parallel planes within the crystal are equal spaced, separated by a fixed distance, d. When the sample is irradiated with monochromatic X-rays, the X-rays are diffracted by the network

of atoms within the crystal structure and beams reflected in the same direction interact with each other. The resultant amplitude depends on the phase shifts of the waves as they move through different distances and interact with different atoms as they penetrate through the crystal planes. The diffraction angle at which positive interference occurs obeys the Bragg diffraction law[37].

$$2d\sin\theta = n\lambda \tag{3.1}$$

Where d is the interplanar distance in a crystal, θ is the diffraction angle, n is an integer known as the order of reflection and λ is the wavelength of the incident x-ray beam. The X-ray diffractogram then consists of the location of the peak at specific diffracting angles 2 θ as expected from Braggs equation. The intensity of the peaks depends on the nature of atoms composing the crystal structure and their relative position within the lattice cell. Each crystalline solid has it unique characteristic X-ray diffraction pattern that may be used as "fingerprint" for comparison. The International Center for Diffraction Data (ICDD) provides the standard powder diffraction patterns of a large number of compounds in the form of JCPDS cards. The structure of an unknown compound can be roughly identified by comparing with the data summarized in these cards. Other information such as crystal structure and space group can also be extracted from the diffractograms.

3.3 N_2 adsorption-desorption studies

3.3.1 Introduction

In heterogeneous photocatalysis process, the adsorption of reactants on the catalyst crystal is a crucial step. Therefore, the characteristics of the catalyst surface that influence the adsorption process are of fundamental importance. Surface area and porosity determine the contact between the reactant and active sites at the catalyst surface. The material with large surface area, the adsorption rate of reactants and the number of active sites at the catalysts surface increase. The study of the gas adsorption properties allows the determination of pore size distribution, surface area and quality of the pores.

The measurement of the surface area of a solid photocatalyst was performed using N_2 sorption techniques. The N_2 molecules are physically adsorbed under controlled condition within a vacuum chamber at its boiling point temperature 77.35 K. The adsorption takes place on the entire particle surface, including the external and internal surface pore surfaces. An N_2 adsorption/desorption isotherm can be obtained by measuring the pressure of the gas introduced into the chamber. The surface area can be calculated from this isotherm by Brunauer-Emmett-Teller (BET) theory.

3.3.2 Adsorption-desorption isotherms

In a gas-solid system, the quantity of gas adsorbed depends on the nature of the gas and the solid. It is proportional to the mass of the adsorbent and depends on pressure and the temperature of the system. For a fixed gas-solid system at constant temperature, the

relationship between the amount of gas adsorbed and its pressure is described through the adsorption isotherms.

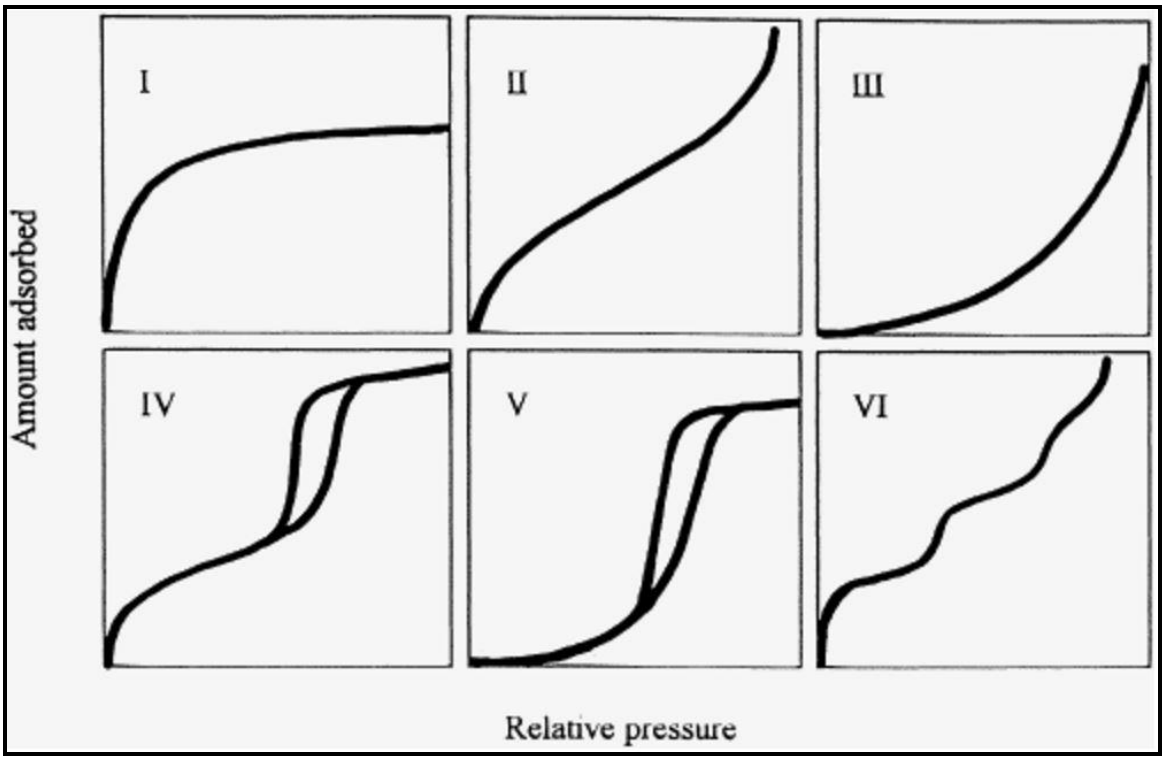

Figure 3.1: The IUPAC Classification of Adsorption Isotherms for Gas–Solid Equilibria.

Fig. 3.1 reported the classification of isotherm for vapor-solid equilibria. Type I isotherm is typical of microporous adsorbents as most microspore filling occurs at relative pressures below 0.1. Type II and type III isotherms identifies the physical adsorption of of gases by non-porous solids with strong and weak adsorbate-adsorbent interactions, relatively[38]. Type IV and V isotherms present a hysteresis loop, which is associated with the presence of mesopores. The hysteresis behavior has been attributed to the capillary condensation [39]. Since the capillary condensation occurs at higher pressures than the capillary evaporation, the hysteresis loop is observed. Type V correspond to weak adsorbate-absorbent interactions and is quite rare.

The hysteresis loops may exhibit different shapes as shown in Fig. 3.2. In type H1, the hysteresis loop is narrow, with the adsorption and desorption branches almost vertical and nearly parallel, indicating a narrow pore size distribution.

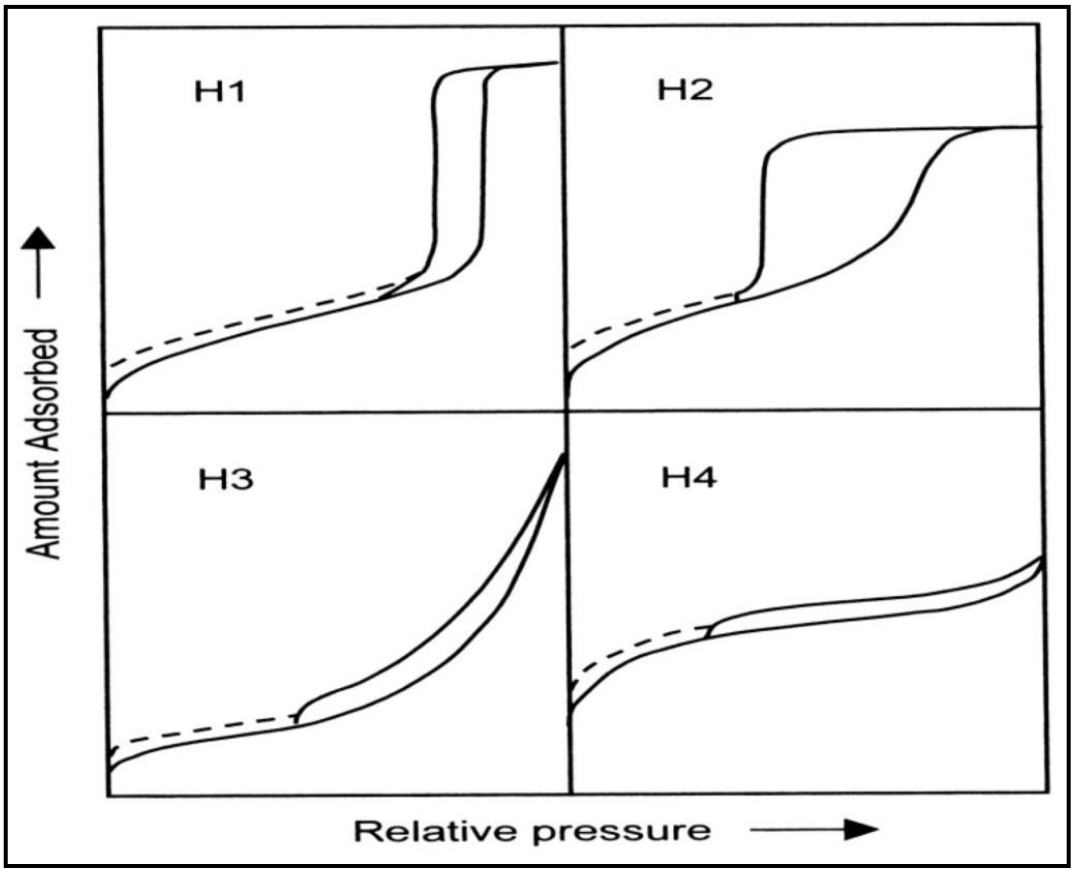

Figure 3.2: The relationship between the pore shape and the adsorption-desorption isotherm.

The type H2 loop is broad with a desorption branch much steeper than the adsorption branch. Type H2 can be found in systems with a broad distribution of pore sizes and pore shapes within the materials. It is believed that this kind of loop results from pores with narrow necks and wide bodies (ink-bottle shape) or when the pores with narrow necks and wide bodies (ink-bottle shape) or when the material has an interconnected pore

network. The type H3 loop does not exhibit any plateau at high relative pressures, indicating significant adsorption. This shape is associated with aggregates of plate-like particles that give rise to slit-shape pores. Finally, the type H4 loop is nearly horizontal and parallel over a wide range of relative pressures and is associated with narrow slit-like pores[40]. In conclusion, Type VI Isotherm occurs rarely and presents steps due to the formation of monomolecular layers. According to the pores diameter d, a solid can be classified in microporous ($d < 2$ nm), mesoporous ($2 < d < 50$ nm) and macroporous ($d > 50$ nm).

In our experiment, the surface area of the photocatalyst was determined by a Micromeritics TriStar 3000 instrument. The powdered samples (0.1 - 0.15 g) were degassed in a sample tube with a slow flow of N_2 for approximately 5 h at 300 °C for those samples calcined higher than 300 °C, and at 100 °C for those samples treated below 300 °C in the sample preparation, to remove any water and contaminants present on the surface. After degassing, the sample was accurately weighed and sample tubes containing the samples were connected to the analysis port of BET instrument. During measurements, the sample tubes were immersed in a Dewar containing liquid nitrogen to maintain it at a constant temperature. Gaseous nitrogen was introduced in small doses under instrument control, and the adsorption/desorption process was followed by measuring the amount of gas adsorbed at various N_2 partial pressure.

3.4 Scanning electron microscopy (SEM)

The scanning electron microscopy (SEM) is an instrument that produces high-resolution images by using electrons instead of light to form an image. Electron microscopy

techniques are intensively used in nanoscience and nanotechnology research to give information about the morphology, topography, composition and crystallographic characteristics of nanoparticles and nanostructured materials. SEM is an introduction to address the resolution limitations of optical microscopy. It is a surface analysis technique that provides images of samples on a microscopic scale. It was used for the investigation

of the morphology of catalyst surface and the evaluation of particle size shape and dimension.

Figure 3.3: Schematic image of a scanning electron microscope with secondary electrons forming the images on the TV screen

In the scanning electron microscope, a beam of electrons is generated in a vacuum. This electron beam is focused into a fine probe and subsequently, raster scanned over a small rectangular area of a sample. As the beam interacts with the sample, it creates various signals (internal currents, secondary electron, photon emissions, etc.). The detection of these secondary electron by scintillation material that produces a flash of light for each electron. Then, the light flashes are detected and amplified by a photomultiplier tube. The image can be formed by correlating the sample scan position with the resulting signal. schematic image of a scanning electron microscopy is given in Fig. 3.3.

The image magnification in the SEM is obtained by controlling the area of the screen to the area scanned of the specimen. Increasing the magnification is accomplished just by scanning the electron beam over the small area of the specimen. The only special requirement is the conductivity and vacuum compatibility for the sample. Semiconductor or insulator samples must be coated either with the gold or carbon thin films.

3.5 Transmission electron microscopy (TEM)

TEM is a microscopic technique used to produce high-magnification images of thin film specimens, which is based on the interaction of high energy electron with matter. In a TEM, a light emission beam of high energy electron is transmitted through a thin film of the sample to give an information about its morphology, crystallography, elemental composition and particle size distribution. It has the capability of giving atomic resolution lattice images and additionally giving chemical information at a spatial resolution of 1 nm or better. However, the resolution power of a microscope is usually controlled by the quality of the lens systems. TEM measurement requires special

preparation to thicknesses, which allow electrons to transmit through the sample. Due to the unique chemical and physical properties of nanomaterials depend on their composition and their structures, TEM offers a means for understanding and characterizing such structures. Furthermore, TEM is a technique that has ability to focus on a single NP in a sample, and directly quantify its electronic and chemical structure. The most important application of TEM is real space imaging of NPs in atomic resolution scale [41]. Furthermore, the detection of the atomic-scale defect and the crystallographic information is possible.

3.6 X-ray photoelectron Spectroscopy (XPS)

XPS is a quantitative spectroscopic technique that measures the chemical state and elemental composition of the elements within a surface of a solid. The base of the technique is a photoelectric effect, which is described by Einstein in 1905, where inner shell electrons or valance are ejected from a surface due to photons absorption of appropriate energy [42].

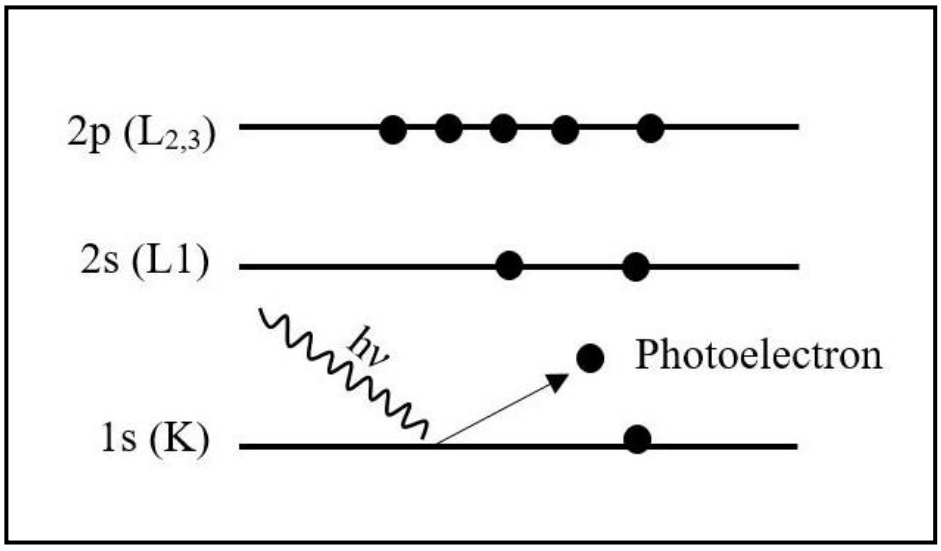

Figure 3.4: Diagram describing the photoelectric effect.

The sample is irradiated in ultrahigh vacuum conditions with soft X-rays. Al Kα (1486.6 eV) or Mg Kα (1253.6 eV) are often used as a monochromatic source of photon. The core electrons are emitted from the specimen (photoelectron), by interaction with the photons.

The photoelectrons ejected are characterized by kinetic energy that depends on its provenance shell. Therefore, kinetic energies are varied for ejected electron which is unique for each element because of the different energies associated with each shell.

The XPS spectra is a plot of counts of the electrons (intensity) versus the binding energy. The binding energies of core electron of an element have a unique value, which allows the chemicals composition identification. Furthermore, the binding energy of the core electrons is affected by its chemical environment. In fact, if the same atom is bonded to different chemical species, the binding energy of its core electron is different. The binding energy variation results in the corresponding XPS peak, ranging from 0.1 eV to 10 eV. This effect is used to identify the chemical status of elements in the surface and is called as chemical shift.

3.7 UV-vis diffuse reflectance spectroscopy (DRS)

DRS is a valuable spectroscopic technique based on light reflection in UV and visible light region by powder sample that probes the absorption of light and band gap energy of the photocatalyst.

In a DRS spectrum, the ratio of the light scattered from an infinitely thick layer and the scattered light from an ideal non-absorbing reference sample is measure as a function of the wavelength λ.

The Kubelka-Munk theory[43] describes the relationship of the diffuse reflection of the sample (R_∞) and absorption coefficient (α) and scattering coefficient (S) for infinitely thick samples.

$$F(R_\infty) = \frac{(1-R)^2}{2R_\infty} = \frac{\alpha}{S} \qquad (3.2)$$

The band gap of semiconductor photocatalyst, which is defined as the minimum photon energy required to excite an electron form the highest occupied molecular orbital to the lowest unoccupied molecular orbital, can be obtained from the diffuse reflectance UV-vis absorption spectra. There are two basic types of electronic transitions, namely direct transitions and indirect transitions. Direct transitions require only that photons excite electrons, while indirect transitions also require concerted vibrations and energy from the crystal lattice (photons). The energy dependence of the absorption coefficient (R) for semiconductors in the region near the absorption edge is given by

$$\alpha \propto \frac{(h\nu - E_0)^\eta}{h\nu} \qquad (3.3)$$

Where hν is the energy of the incident photon, and E_0 is the optical absorption edge energy. The exponent depends η depends on the type of optical transition caused by photon absorption. In crystalline semiconductors, where crystal momentum is conserved and electron transition obey well-defined selection rules, η is ½, 3/2, 2 and 3 when the transitions are direct-allowed, direct-forbidden, indirect-allowed, and indirect-forbidden, respectively[44].

In the diffuse reflectance experiments, UV-vis reflectance data cannot be used directly to measure absorption coefficients (R) because of scattering contributions to the reflectance

spectra. Scattering coefficients, however, depend weakly on energy and $F(R\infty)$ can be assumed to be proportional to the absorption coefficient within the narrow range of energy containing the absorption edge features. Then, a plot of $(F(R\infty).h\nu)^{1/\eta}$ vs $h\nu$ can be used to determine the absorption edge energy.

In this work, the diffuse reflectance spectra were taken using a Shimadzu UV-2450 UV-Visible spectrophotometer with diffuse reflectance accessory ISR-240A. $BaSO_4$ was used as reference. The band gaps were obtained from plots of $(F(R\infty).h\nu)^2$ versus the energy of light for indirect bang gap semiconductors.

CHAPTER 4

Photocatalytic Degradation of Herbicide (Atrazine) using Surface Plasmon Resonance Induced Ag-WO_3/SBA-15 Composite in the Visible Spectral Region

4.1 Introduction:

Although water is one of the most essential natural resources to sustain life on earth, the grim reality is that the level of ground water and the number of water bodies are fast declining globally and the condition becomes even more menacing as various human activities recklessly pollute the scarcely available water resources. Like industries, the farming and agricultural sectors also significantly contribute to water pollution by the extensive use of persistent organic pollutant (POPs) in the form of fertilizers, insecticides and herbicides[45]. Atrazine ($C_8H_{14}ClN_5$; IUPAC name: 1-Chloro-3-ethylamino-5-isopropylamino-2,4,6-triazine is a well-known and the most extensively used herbicides in agriculture, classified as POPS owing to the low biodegradability and long half-life in water (between 30 and 100 days). In addition, the solubility (30 mg/l at 20 °C) and mobility of atrazine in water are relatively high and this leads to seep into the ground water and blend with the surface water[46]. Hence in many countries atrazine is the most commonly detected herbicides in surface and ground water and is considered as a possible human carcinogen and the cause of the decreased fertility and semen quality in men living in the agricultural area[47,48].

The conventional water treatment processes like coagulation, filtration method using ferric chloride, aluminum sulfate and lime soda, adsorption based methods using granular activated carbon and powder activated carbon, ozonation, membrane filtration for the elimination of atrazine have proven to be less effective[49]. The long duration of UV irradiation in the presence of hydrogen peroxide yielded a slightly better decomposition of atrazine but did not result in complete mineralization[50]. The photocatalysis has been a promising method employed for the elimination of organic, inorganic and microbial pollutants present in water. This method is based on the advanced oxidation and reduction processes mediated by photo-generated electrons and holes to generate highly hydroxyl radicals ($^{\bullet}OH$) and superoxide anion ($O_2^{\bullet-}$), which in turn oxidize organic pollutant into CO_2 and inorganic ions as a final degrading product[51].

Fujishima published his pioneering and remarkable work on photocatalysis, in 1972, where TiO_2 was used as a catalyst for water splitting[8]. Since then, there has been a widespread research interest in the synthesis and applications of doped, co-doped, and composites of TiO_2 for various photocatalytic applications. This knowledge base and the advent of nanomaterials promoted photocatalysis as one of the most effective, cheap and environmentally friendly methods to deal with burning environment problems and ever increasing energy requirements[52]. Many semiconductor materials such as TiO_2 nanowires[53,54], $Pt/AgVO_3$ nanowires[55], and TiO_2 superficially modified with metallic NPs[56] have been investigated for the degradation of Atrazine. Although TiO_2 has become popular due to the low cost, high thermal and chemical stability, the larger band gap of this material really restricts its use only in the UV region. In order to harness the abundant visible solar radiation, research into the synthesis of photocatalyst with suitable

band gap energy, high mobility of charge carriers and appropriate surfaces area are important. By controlled nitrogen insertion in titanium dioxide, the band gap is red-shifted to visible range so that the material shows reasonably good photocatalytic degradation of atrazine[57].

Tungsten oxide (WO_3) is an n-type semiconductor with a short band gap energy (2.8 eV), high stability, a good electron transporting property and corrosion free and all these positive attributes make this material one of the most sought after photocatalyst[58]. Although the short band gap energy of WO_3 makes this material visible light active, the consequent increase in the electron-hole recombination prevents it from being a naturally good photocatalyst[59–61]. This increased electron-hole recombination, small surface area and poor adsorption of organic pollutant onto its surface naturally reduce the photocatalytic degradation efficiency of WO_3. If these deficiencies can be rectified, WO_3 can function as an excellent photocatalyst, capable of harnessing solar radiation in the visible region for a various of energy and environmental applications. Among the various porous materials, Santa Barbara Amorphous (SBA) type material or (SBA-15) silica has been widely used as a catalytic support to increase the effective surface area and also to increase the adsorption and electron transport properties[62]. SBA-15 is a mesoporous silica material characterized by uniform hexagonal channels of the size of 5-30 nm and the wall thickness of 3.1-6.4 nm and for this unique shape and size, SBA-15 is commonly used as a support in photocatalysis[63].

The semiconducting materials loaded with Nano-sized metals like Au, Fe, Co, Ni, Cu, Zn, Mn and Ag[58,64–72] on its surface can restrain the recombination of the photo-induced charge carriers. Generally, with light irradiation, the electrons from the valence band of

the semiconductor transfer to the conduction band leaving a hole behind in the valence band. However, when the semiconductor is coupled with noble metals, the electrons from the semiconductor transfer to noble metal particles because the energy of the Fermi level of the semiconductor is higher than that of noble metal. Hence, the photogenerated electrons accumulate on the noble metal, which serves as trap centers to facilitate charge separation, which is crucial for photocatalytic activity. Another advantage of having the nanostructured noble metals is the induction of surface plasmon resonance due to the collective oscillation of photo-generated electrons in resonance with the incident radiation[73]. This surface Plasmon resonance enhances the photocatalytic activity by transferring the plasmonic energy to excite the electron–hole pairs, or directly generating the hot electrons[74–76].

In this work, we improved the photocatalytic function of WO_3 by introducing two modifications: (i) enhancing its surface area by impregnation onto SBA-15 template and (ii) by deposition of the sample with the noble metal Ag to reduce the electron-hole pair recombination and to induce surface plasmon resonance for enhancing the generation of charge carriers. The modified WO_3, labeled as Ag-WO_3/SAB-15 was tested as a photocatalyst for the degradation of atrazine in water and its photocatalytic activity is compared with the commercial WO_3 and synthesized WO_3/SAB-15. The effect of varying Ag concentartion Ag conentration on the WO_3/SBA-15 was investigated. The synthesized materials were characterized morphologically and optically correlated to their photocatalytic performance.

4.2 Experimental Methods

4.2.1Chemicals

The required chemicals like standard atrazine (97.5% purity analytical grade), Tetraethyl orthosilicate (TEOS), Methanol (HPLC grade), Poly (ethylene glycol)-poly (propylene glycol)-poly (ethylene glycol) (P-123), polydiallydimethyl ammonium chloride and Silver nitrate were obtained from Sigma-Aldrich.

4.2.2 Synthesis of the catalyst

For the synthesis of SBA-15, a 2.0 g of P-123 was dissolved in 75 mL of HCl (1.6 M) aqueous solution. The resultant solution was stirred and heated at the temperature of 40 °C for 3 hours. Then, 4.5 g of TEOS was added into the P-123/ HCl solution and stirred for another 24 hours. The slurry thus obtained was transferred into an autoclave and aged for 24 hours at the temperature of 100 °C. The final product was collected by centrifugation, washed with water for three to four times, dried at the temperature of 60 °C overnight and finally calcined for 12 hours at the temperature of 550 °C.

In order to obtain the SBA-15 loaded with 10 % WO_3, typically 0.5 g SBA-15 was added 10 mL of polydiallydimethyl ammonium chloride (0.5 wt percentage solution) and stirred at room temperature for 3 hours. A measure of 61 mg of ammonium tungstate was dissolved in water by heating and then added into the SBA-15 solution. This mixture was stirred for three hours, dried at the temperature of 70 °C and finally calcined at the temperature of 500 °C for 3 hours. The similar procedure was used to synthesize 20%, 30%, 40% WO_3/SBA-15.

For Ag deposition on WO_3/SBA-15, only 40% WO_3/SBA-15 was selected. In order to obtain 0.5 % Ag/ 40 % WO_3/SBA-15, an appropriate amount of 40% WO_3/SBA-15 was dissolved in 5 mL of water, sonicated for 15 minutes and then 900 μL of $AgNO_3$ (0.01 M) aqueous solution was added. The slurry was stirred and heated at 60 °C until it was dry. The dried powder was calcined at 300 °C for 3 hours. Similar procedure was followed to obtain other concentrations of Ag in 40 % WO_3/SBA-15.

4.3 Characterization of Material

The phase and crystallinity of the synthesized materials were investigated by XRD (Siemens D5005) equipped with Cu anode and variable slits. The XPS profiles of the samples were acquired by survey scan using X-ray Photoelectron Spectrometer (PHI 5000 Versa Probe II, ULVAC-PHI Inc.). The morphology and the microstructure of the synthesized materials were studied by HR-TEM (JEM2100F, JEOL, operated at 200 KV). The diffuse reflectance spectra (DRS) were taken using a Shimadzu UV-2450 UV-Visible spectrophotometer. The photoluminescence (PL) emission spectra were acquired by spectrofluorometer (Horiba Jobin Yvon), using the Xenon lamp as an excitation source and all the samples were excited with 365 nm wavelength light radiation, and the emission spectra were recorded in 400 to 700 nm range. A micrometrics accelerated surface area and porosimeter (ASAP 2020) system was used to measure nitrogen adsorption-desorption of the catalysts. The system is equipped with dedicated software which uses conventional analysis such as Brunauer-Emmett-Teller (BET) and Barrett-Joyner-Halanda (BJH) methods for the determination of the textural properties, like specific surface area and pore size distribution respectively.

4.4 Photocatalytic activity

The photocatalytic testing was carried out in a beaker containing 25 ml of 20 ppm atrazine solution and 25 mg catalyst. The suspension was magnetically stirred for 15 min in the dark to establish the adsorption-desorption equilibrium of atrazine at the surface of the catalyst. The suspension was irradiated with a broadband light source (450 W Xe arc lamp) fitted with a neutral density optical filter to allow light of wavelength above 400 nm. The reaction temperature was maintained at 25 ± 1 ℃ and irradiated suspension was collected at regular time intervals through 0.22 µm nylon filters to remove any catalyst particles in the test solution. The concentration of atrazine in the samples was quantified using a high-performance liquid chromatography (HPLC, Dionex UltiMate 3000) at wavelength of 220 nm. A C18 column (120 x 3.6 mm, particle size 3 µm) was employed. The elution phase was a mixture of methanol/water (60:40, v/v) at a flow rate of 0.20 ml/min and the injection volume was 10 µL. Under these conditions, the retention time of atrazine was 1.5 min.

4.5 Results and Discussion

4.5.1 Morphological Characterization

Fig. 4.1 shows wide-angle XRD pattern of WO_3/SBA-15 with different concentrations of WO_3 in SBA-15 along with that of pristine SBA-15. In the case of pristine SBA-15 in figure 1a, the broadband at 2θ = 23.5° in the XRD pattern corresponds to the amorphous silica walls[61] and as the concentration of WO_3 increases, very sharp peaks emerge from

the amorphous SiO_2 substrate, indicating good crystallinity and high purity of the as-generated WO_3. In addition, it can be noticed that in Fig. 4.2b, corresponding to the XRD patterns of 10% WO_3 / SBA-15, the characteristics peaks of WO_3 are barely visible due to the low concentration, indicating the amorphous nature of the composite.

The inset in Fig. 4.1 shows the low-angle powder X-ray diffraction (XRD) patterns of the sample of 10%, 20%, 30% and 40% of WO_3 loaded on SBA-15 along with that of SBA-15 itself. In the inset figure the three characteristic peaks at 2θ = 0.8°, 1.53° and 1.75° are evident, of which the first peak corresponds to the mesoporosity of SBA-15, while the other two small characteristic peaks correspond to highly ordered hexagonal shape which can be interpreted as 100, 110 and 200 reflected of P6 mm space group of SBA-15[77]. After WO_3 of different concentrations loaded on SBA-15, ordered mesoporous structure is well retained. However, there was a gradual shift of the peak position to a slightly larger angle, which indicates that some WO_3 might enter the pore channels of the SBA-15 substrates. Fig. 4.2 depicts the wide-angle XRD pattern of 40 % of WO_3/SBA-15 (Fig. 4.2a) and that of two different concentrations of Ag (0.5% and 1 %) added to it. The incorporation of Ag in 40% of WO_3/SBA-15 did not result in any obvious change in the XRD patterns, which might be due to the homogenous distribution of Ag nanoparticles in the composite, the low Ag concentrations of Ag and / or their small sizes. However, in the low angle XRD patterns (inset), the peak intensities decrease with the increasing concentration of Ag, indicating that the surface of WO_3/SBA-15 is covered by the Ag nanoparticles.

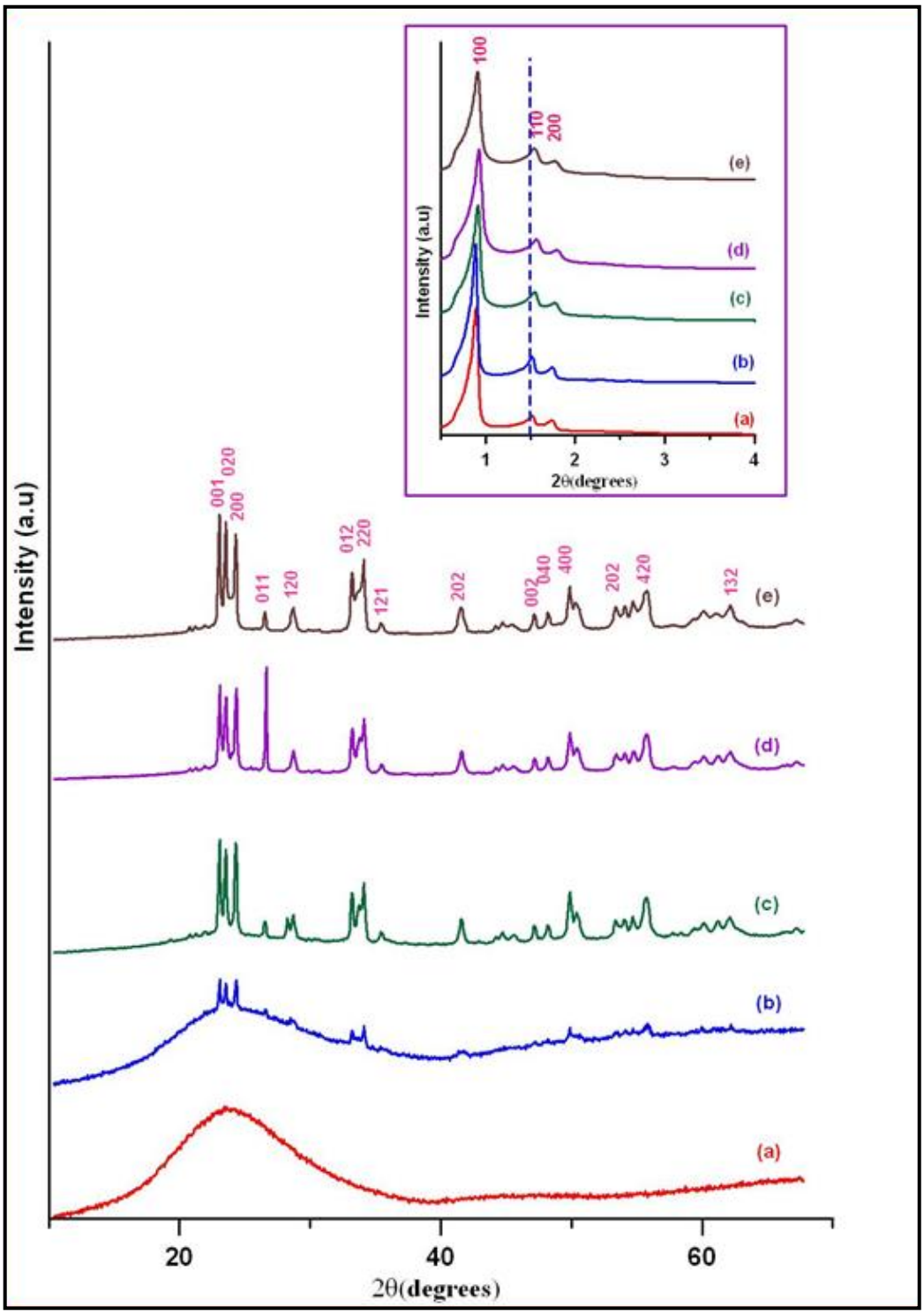

Figure 4.1: XRD patterns of (a) SBA-15 (b) 10% WO_3/SBA-15 (c) 20% WO_3/SBA-15 (d) 30%WO_3/SBA-15 and (e) 40% WO_3/SBA-15. Inset shows the small-angle XRD for the same composites in the same order (a) to (e).

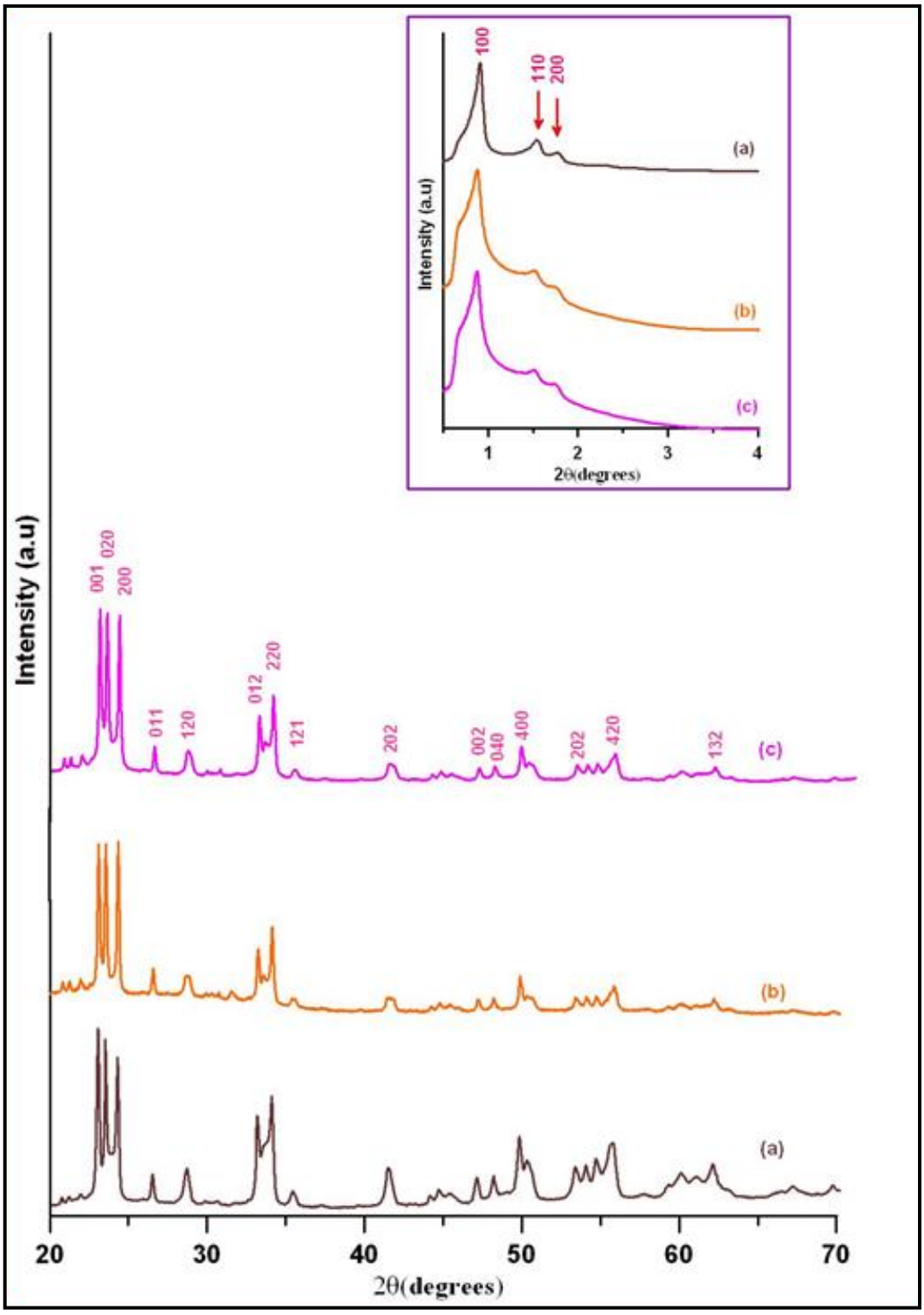

Figure 4.2: XRD patterns of Ag-loaded WO_3-SBA-15 composites (a) 40% WO_3/SBA-15 (b) 0.5 % Ag in 40% WO_3/SBA-15 and (c) 1 % Ag in 40% WO_3/SBA-15. Inset shows the Small-angle XRD for the same composites in the same order (a) to (c).

However, in the small-angle XRD patterns for different concentrations of Ag in 40 % of WO_3/SBA-15 shown in the inset of Fig. 4.2, we can notice that the XRD peak intensities decrease with the increased concentration of Ag. This indicates that the surface of WO_3/SBA-15 is covered by the Ag NPs, which is substantiated by SEM-EDX mapping which shows the well distribution of Ag NP on the surface of the composite, which will be discussed in the following section (Fig. 4.3).

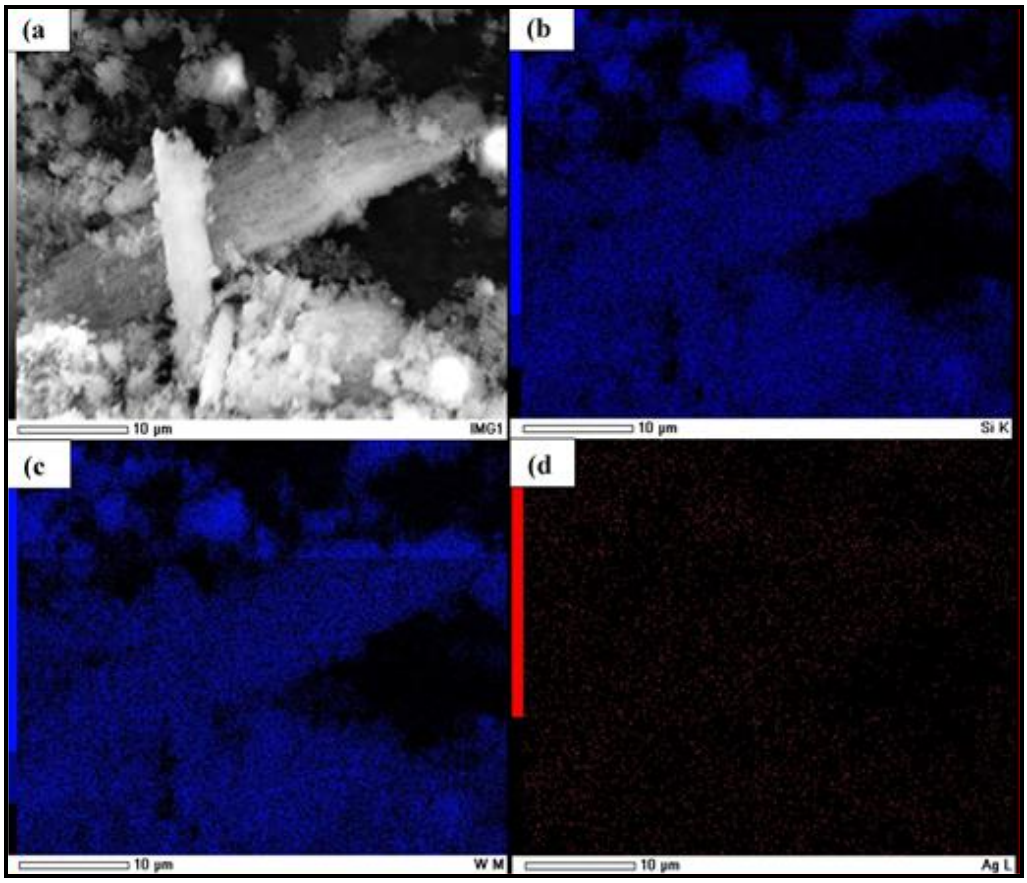

Figure 4.3: (a) SEM image of 1 % Ag-WO_3/SBA-15 particle, (b) SEM-EDX elemental mapping image of Si(K) on this area, (c) SEM-EDX elemental mapping image of W(M) on this area, (d) SEM-EDX elemental mapping image of Ag(L) on this area.

From HR-TEM of 40 % WO_3/SBA-15 (Fig. 4.4a-b), the mesoporous channels of SBA-15 can be clearly discerned. While WO_3 deposited in the pore channels cannot be observed, larger WO_3 particles of ~ 100 – 200 nm are present at the external surface of the SBA-15 support. The micrographs of 1% Ag-WO_3/SBA-15 show spherical Ag nanoparticles of less than 10 nm (Figure 4c-e). The d-spacing of 0.231 nm in the TEM image corresponds to (111) plane of face-centered cubic silver structure.

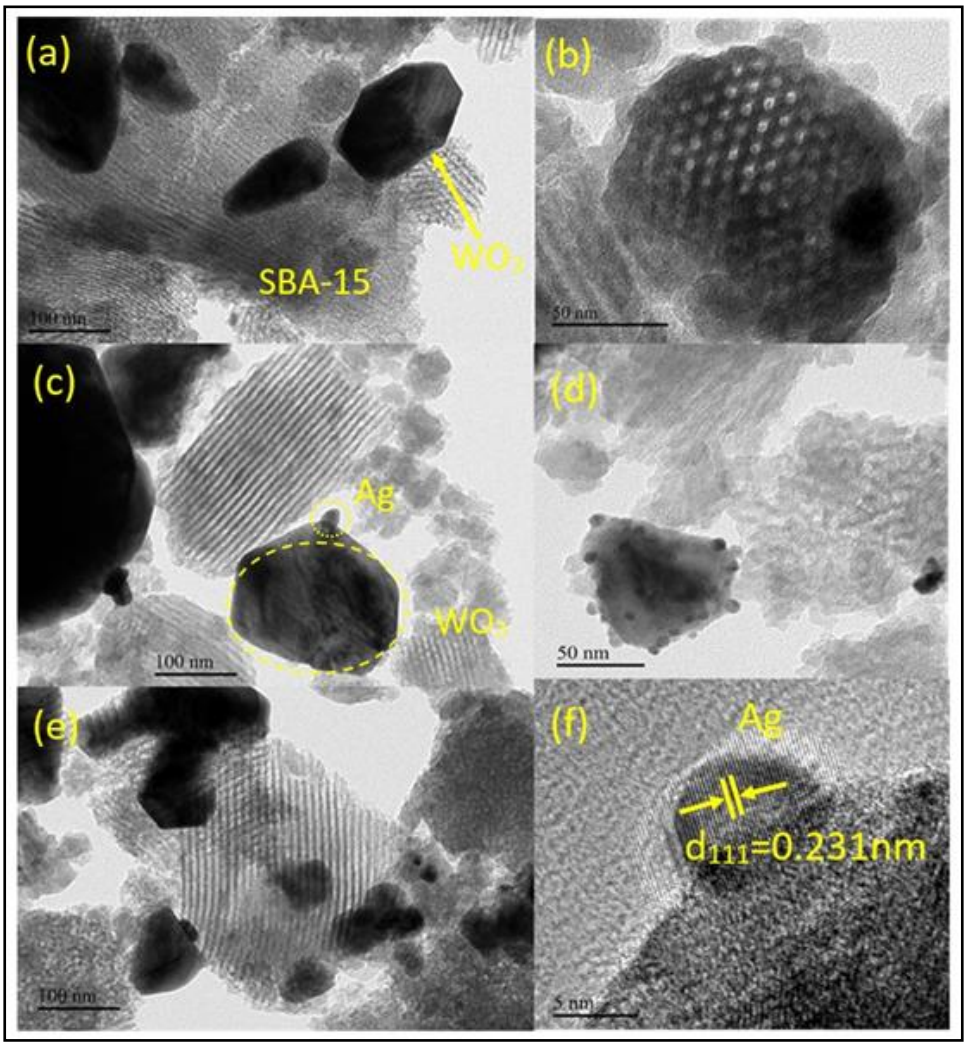

Figure 4.4: TEM images of low and high magnification mesoporous (a) 40% WO_3/SBA-15 (c-e) 1% Ag in WO_3/SBA-15 (f) d-spacing.

XPS survey and the high-resolution scan for Ag-WO_3/SBA-15 is presented in Fig. 4.5 and it is found from the entire XPS spectrum in Fig. 4.5a that the composite consists of Ag, W, O and Si and the binding energy at 284.78 eV is for C 1s is from the calibration. The two peaks at 36.8 eV and 38.5 eV shown in Fig. 4.5b originate from W^{6+} 4 $f_{7/2}$ and 4 $f_{5/2}$, respectively and this suggests that the tungsten in the tungsten oxide sample exists as W^{6+}. Two prominent peaks at 368.34 and 374.34 eV with a 6 eV spin−orbit splitting value (Fig. 4.5c) are the characteristic of Ag^0 species in the Ag-WO_3/SBA-15[78].The formation of Ag^0 can be attributed to phot-reduction although the presence of Ag2O cannot be excluded. The peak located at 533.8 eV in Fig.4.5 resulted from the O 1s state.

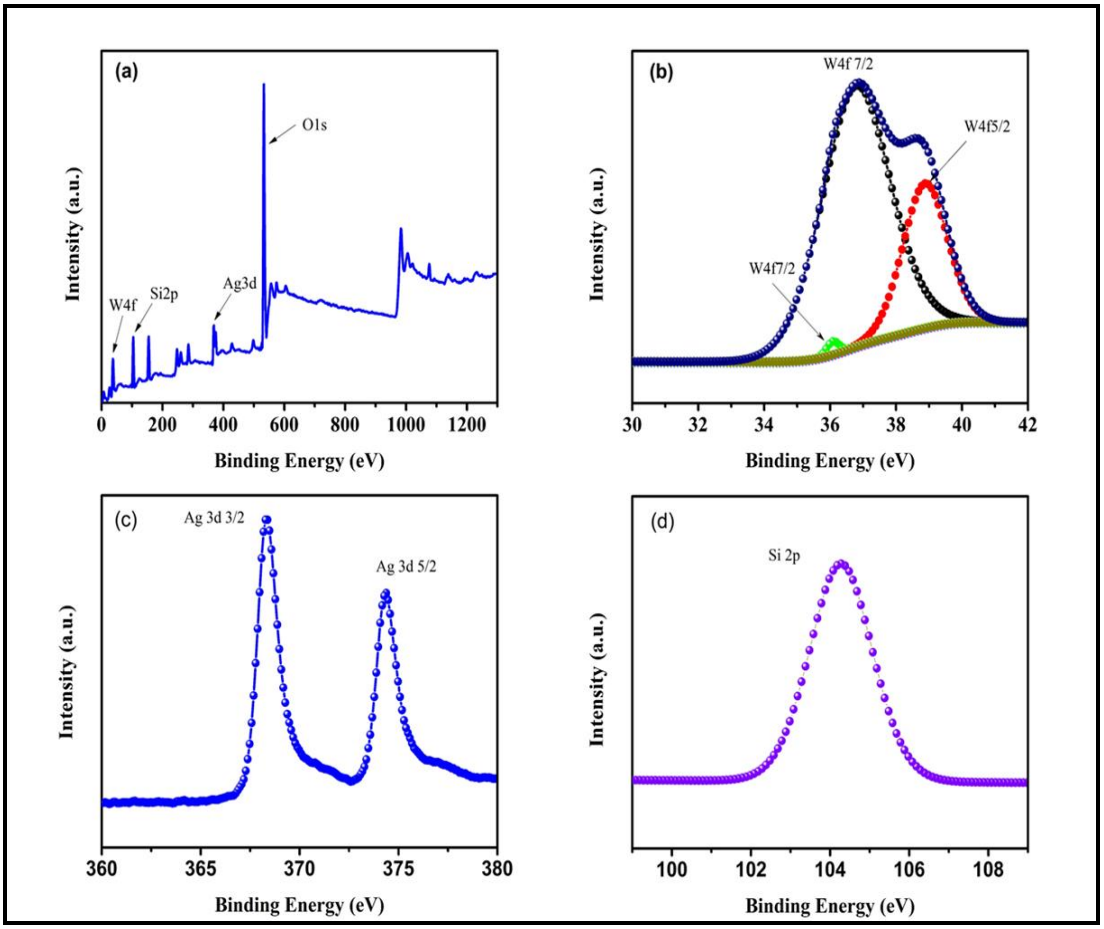

Figure 4.5: XPS spectra of (a) survey of the sample, (b) W 4f, and (c) Ag3d (d) Si 2p of the 0.5% Ag-WO_3/SBA-15.

BET and BJH analysis for specific surface areas, pore sizes and pore volumes of WO_3/SBA-15 and Ag-WO_3/SBA-15 were carried out and the results are presented in Fig. 4.6 and in Table 4.1. These figures depict the nitrogen adsorption-desorption isotherms and the corresponding pore diameter versus pore volume plot.

Table 4-1: Properties of SBA-15, WO_3/SBA-15, and Ag-WO_3/SBA-15 samples.

Sample	*S_{BET} (m^2 g^{-1})	*Vp (cm^3 g^{-1})	Band gap (eV)	Rate constant (K) min^{-1}
SBA-15	603	0.93	-	-
10% WO_3/SBA-15	542	0.88	3.0	0.001
20% WO_3/SBA-15	560	0.87	2.5	0.010
30% WO_3/SBA-15	495	0.75	2.5	0.021
40% WO_3/SBA-15	344	0.56	2.4	0.024
0.5% Ag/40% WO_3/SBA-15	231	0.43	1.7	0.036
1.0% Ag/40% WO_3/SBA-15	208	0.43	1.7	0.065

* Vp pore volume, S_{BET} surface area

From the figures, it is quite clear that all samples manifest the characteristic broad hysteresis loop of type IV according to IUPAC convention and these results suggest that the samples are mesoporous in nature have uniform cylindrical geometry. As the content of WO_3 in SBA 15 increases, a systematic decrease of pore volume and pore diameter are observed (Table 4-1). However, the decrease in surface area cannot be related to the amount of WO_3 particles alone and the decrease in pore volume could be due to increasing of pore wall thickness, indicating that successful incorporation of WO_3 particle inside the mesoporous channels. With the addition of Ag, the surface area further

decreases to 208 – 231 m^2g^{-1} and the total pore volume dropped from 0.56 to 0.43 cm^3 g^{-1} . The mean pore diameter of the samples with Ag deposition is slightly smaller than the WO_3/SBA-15 support, showing that some of the Ag nanoparticles could have blocked the smaller pore channels.

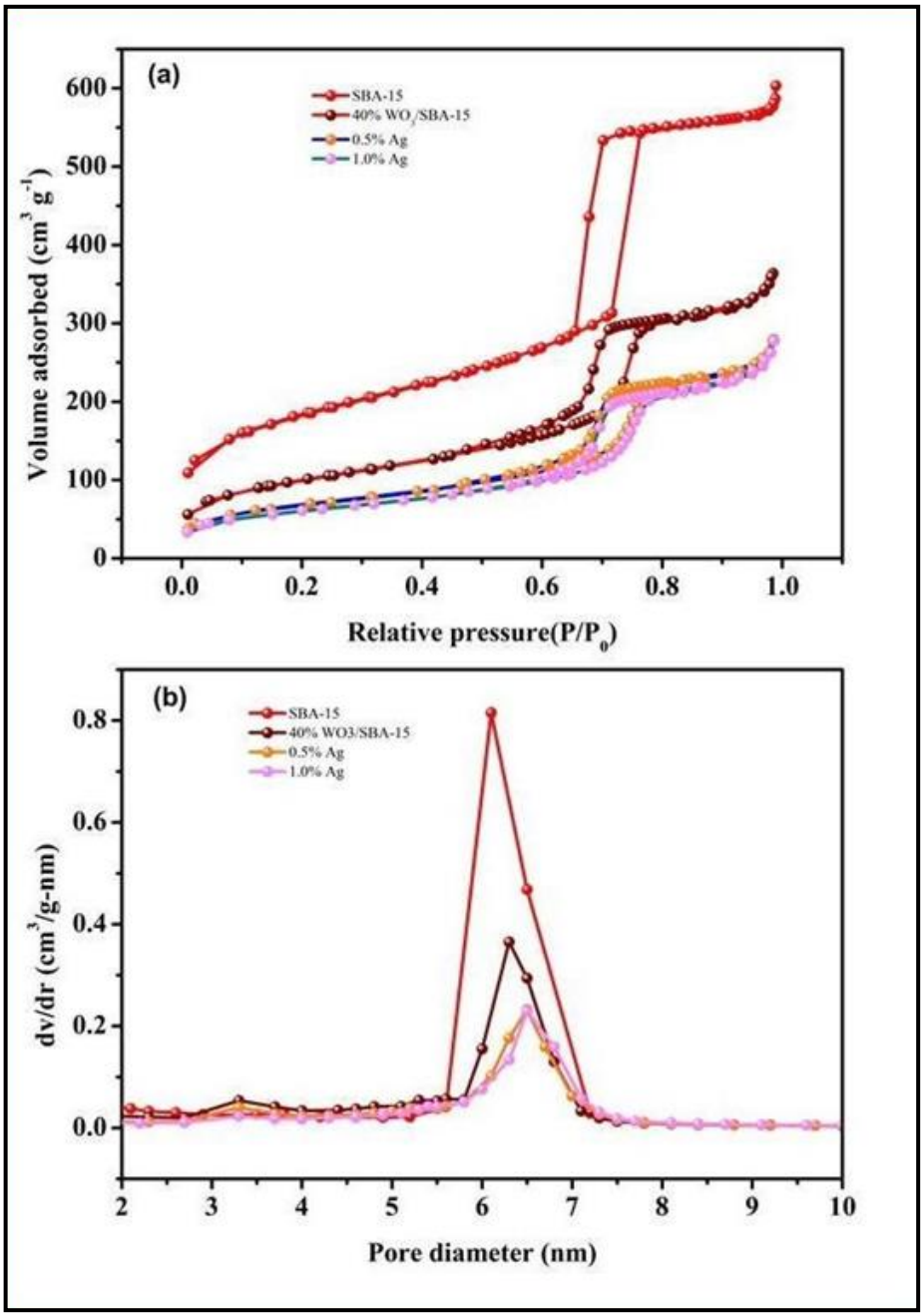

Figure 4.6: (a) N_2 adsorption-desorption isotherms of SBA-15, 40% WO_3/SBA-15, 0.5% Ag in 40% WO_3/SBA-15 and 1% Ag in 40% WO_3/SBA-15 (b) the corresponding pore size distribution curves.

4.5.2 Optical Characterization

Fig. 4.7 shows the optical absorption spectra of WO_3/SBA-15 with different WO_3 content, represented in terms of Kubelka–Munk (K.M) function[43,79] transformed from the diffuse reflectance and Fig. 4.8 shows the same for Ag-WO_3/SBA-15 with different Ag concentrations on 40% WO_3/SBA-15. It is quite clear from the figure 8a that the absorption spectra (represented as K.M function) for pure SBA-15 has no absorbance at all. However, SBA-15 loaded with 10% WO_3 shows absorption in the 200-400 nm region. The absorption band broadens and shifts to higher wavelength with increased WO_3 content. With the addition of 1% Ag on 40% WO_3/SBA-15, the absorption edge is further red shifted to beyond 660 nm (Fig. 4.8). This increased absorption in the higher wavelength region upon deposition of Ag NPs can be due to the surface plasmon resonance effect arising from charge transfer between the WO_3 species and Ag NPs[80].

In the insets of Fig. 4.7 and Fig.4.8, the band gap energies of all the synthesized materials were graphically estimated through the Tauc plot[81], where the Kubelka Munk function is substituted for absorbance as these functions are directly related. For an indirect band gap material, F(R) is proportional to $(E-Eg)^2/E$, where E is the photon energy and Eg is the band gap energy[82] and by plotting $(F(R) *E)^{1/2}$ versus E, the band gap energy Eg can be directly estimated from the X- intercept of the plot.

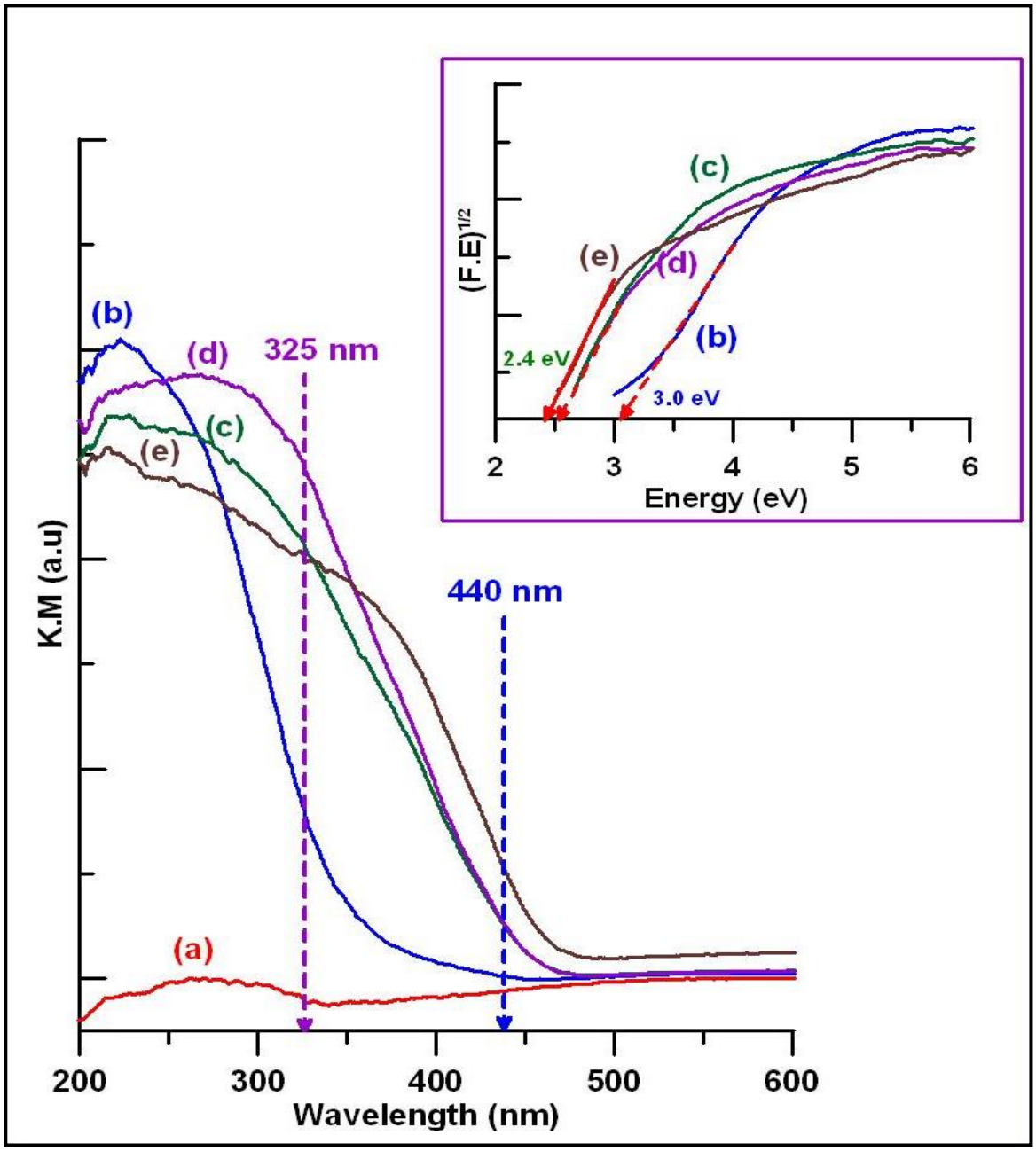

Figure 4.7: UV-VIS diffuse reflectance spectra represented as Kubelka-Munk Function for (a) SBA-15 (b) 10% WO_3/SBA-15 (c) 20% WO_3/SBA-15 (d) 30% WO_3/SBA-15 and (e) 40% WO_3/SBA-15. Inset shows the Tauc plots for the same composites in the same order (b) to (e).

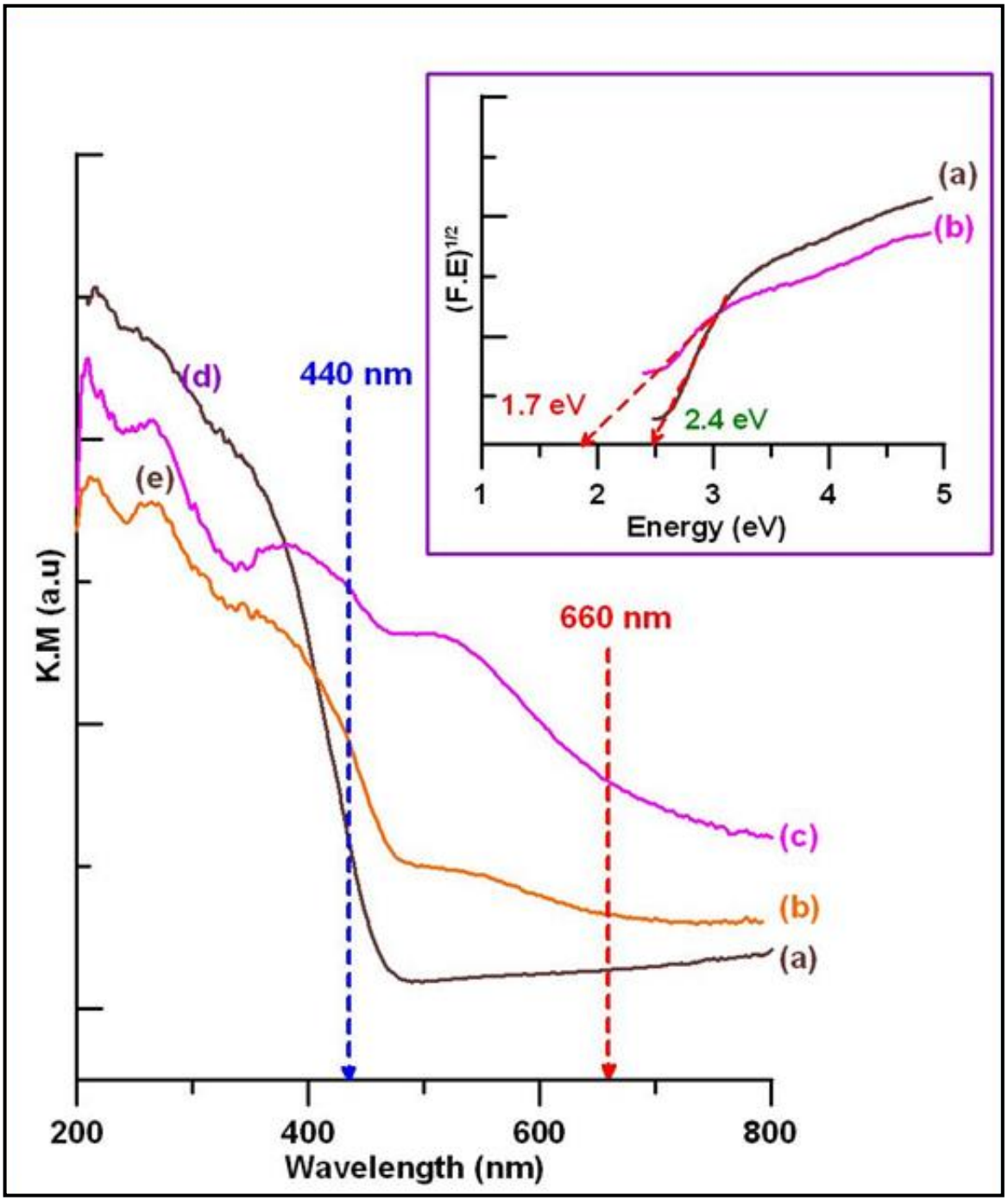

Figure 4.8: UV-VIS diffuse reflectance spectra represented as Kubelka-Munk Function for (a) 40% WO_3/SBA-15 (b) 0.5 % Ag in 40% WO_3/SBA-15 (c) 1 % Ag in 40% WO_3/SBA-15. Inset shows the Tauc plots for the same composites in the same order (a) to (b).

The inset of Fig. 4.7 shows the Tauc Plot for WO_3/SBA-15 with different WO_3 contents where the shrinking of the band gap energy from 3 eV to 2.4 eV with the increase of WO_3 content from 10% to 40 % in WO_3/SBA-15. However, from the inset of Fig. 4.8 it is quite clear that with the addition of Ag into WO_3/SBA-15, the band gap energy is drastically reduced to 1.7 eV for both 0.5 % Ag and 1% Ag in the composite of 40 % WO_3 in WO_3/SBA-15. The band gap energies of all the catalysts are listed in Table 4-1.

Fig. 4.9 depicts the photoluminescence spectra of two different concentrations of Ag in 40 % WO_3 in WO_3/SBA-15 and in the absence of Ag, the intensity of the PL spectra is quite high and with the increased concentration of Ag doping the intensity reduces. The reduced PL intensity is attributed to the reduction in the electron-hole recombination achieved due to the electrons trapping ability of Ag from the formation of Schottky barrier. Fermi level of the semiconductor is higher than that of noble metal and hence the photogenerated electrons accumulate on the noble metal, which serves as trap centers and facilitates the charge separation. The function of Schottky junction is not only to effectively separate the photo-generated charge carriers but also to quickly move the separated photoelectrons, which effectively restrains photogenerated electron-hole recombination. Thus, the Ag doping in WO_3/SBA-15 brought about the essential features required for a good photocatalyst like its ability to work in the visible region and reduced electron-hole recombination in addition to the increased surface area.

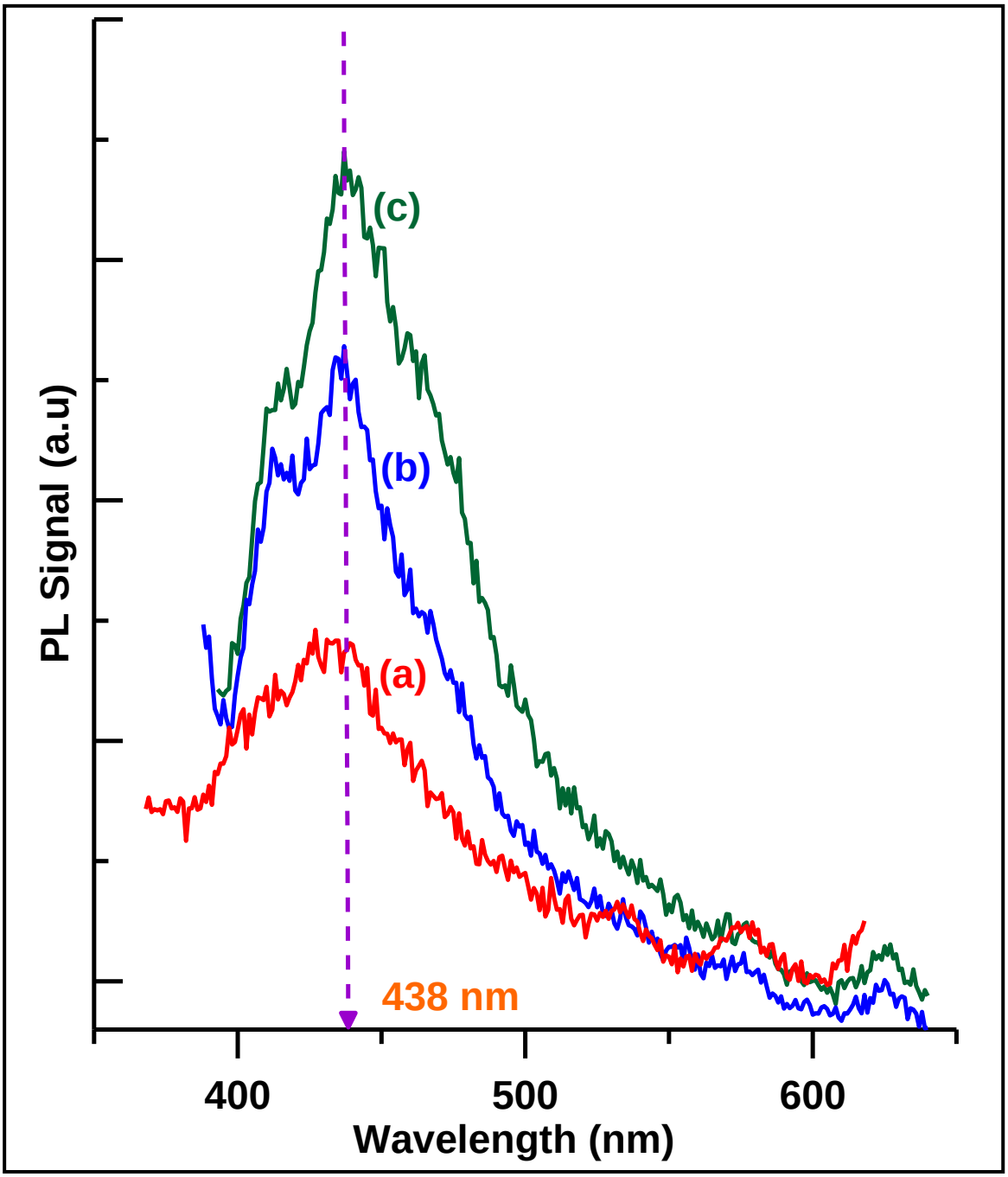

Figure 4.9: Photoluminescence spectra of (a) 1 % Ag in 40% WO_3/SBA-15, (b) 0.5 % Ag in 40% WO_3/SBA-15 (c) 40% WO_3/SBA-15.

4.6 Evaluation of Photocatalyst for the Degradation of Atrazine

The photocatalytic activity of Ag-WO_3/SBA-15, in the process of photocatalytic degradation of atrazine in the presence of visible radiation was studied and its performance is compared with WO_3/SBA-15 and SBA-15. For this 25 mL of 20 ppm atrazine solution was added with 25 mg of the catalyst and the resultant suspension was magnetically stirred for 15 min in the dark to confirm the complete adsorption-desorption equilibrium of atrazine in the surface of the catalyst. This suspension was irradiated with a broadband light source (450-W Xe arc lamp) and the neutral density optical filter to allow the light of wavelength above 400 nm. The reaction temperature was maintained at 25 ± 1˚C and irradiated suspension was collected in a regular time interval through a 0.22 µm nylon filters to remove the particles of catalyst in the test solution. The quantification of atrazine was carried out using HPLC through direct injection. The zero-time reading was obtained from the suspension kept in dark for each catalyst. Fig. 4.10 A shows the decay curve of atrazine in the presence of WO_3/SBA-15 with different WO_3 contents and Ag-WO_3/SBA-15 with different Ag concentrations in 40% of WO_3 in SBA-15 under visible radiation. The y-axis of the decay curve presented in Fig.10A is the ratio of the concentrations of irradiated samples taken (C) at regular time interval to the initial concentration (C_0), while the y-axis of decay curve presented in Fig. 4.10B is the linear version of Fig. 4.10A (ln C/C_0), assuming that the decay is exponential in nature. The purpose of the decay curve presented in Fig. 4.10B is to deduce comparable decay constant (k in the unit of $minute^{-1}$) values to quantify the efficiency of each catalyst.

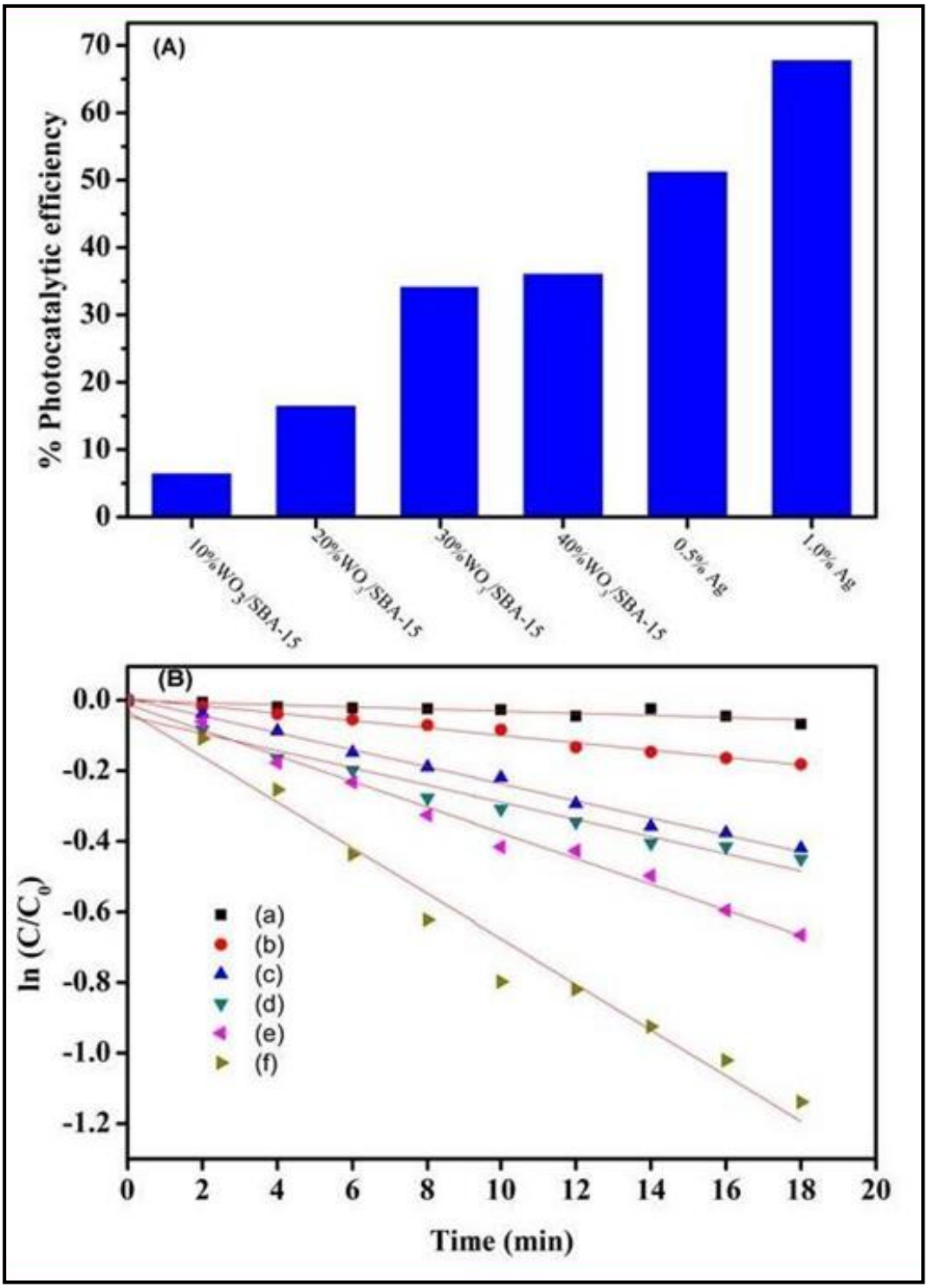

Figure 4.10: (A) Degradation efficiency of atrazine (B) Photocatalytic degradation plots.

To start with, the decay curves in Fig. 4.10A (a) represents the photocatalytic decay of atrazine in the presence of 10%WO_3/SBA-15, where the degradation of atrazine is negligible even after 120 minutes of irradiation with the decay constant as small as 0.001 $minute^{-1}$. With the increased content of WO_3 in SBA-15, used for the degradation process (Fig. 4.10 (b-d)), the photocatalytic decay curves of atrazine become steeper with increased decay constants going up to 0.024 $minute^{-1}$ when 40% WO_3 is added to SBA-15. This increased photocatalytic activity of WO_3/SBA-15 with increased WO_3 content can be attributed to two characteristics discussed in the previous sections: one the increased surface area coupled with an adequate quantity of WO_3 in SBA-15 and second the increased UV light absorption of 40% WO_3/SBA-15 observed in the optical studies. As it is clear from Table 4-1 that the surface area decreases with the increase of WO_3 content in SBA-15, which is not favorable for the photocatalytic activity. However, the photocatalytic activity of 40% WO_3/SBA-15 is higher than the one with lower contents of WO_3 in SBA-15. This is because, in the case of 40% WO_3/SBA-15, it possesses not only the optimum content of WO_3 but also has an optimum balance between the WO_3 content and the surface area even though the surface area observed for it is smaller than the other catalysts. When WO_3 content in SBA-15 is more than 40%, the photocatalytic activity becomes lower due to the drastic reduction in the surface area even though the WO_3 content is more in the SBA -15 template.

Hence 40% WO_3/SBA-15 catalyst is used for Ag loading to further enhance the photocatalytic reduction of atrazine. Fig. 4.10A (e-f) show the photocatalytic decay curves of two concentrations of silver loaded (0.5% and 1%) in 40% WO_3/SBA-15 and

we can notice a drastic enhancement of photocatalytic degradation of atrazine with 1% Ag-WO_3/SBA-15 with the decay constants reaching as high as 0.065 $minute^{-1}$. From Table 4-1 we can observe that with Ag doping on 40% WO_3/SBA-15, the surface area and the volume further reduces, which is supposed to hamper the photocatalytic activity. However, the red-shifting of the band gap energy towards the attractive visible region, enhanced visible absorption and the surface plasmon resonance brought about by the introduction of Ag into WO_3/SBA-15 are the key factors that can be attributed to the enhancement of photocatalytic reduction of Atrazine with 1% Ag -WO_3/SBA-15 as a photocatalyst under visible light. Fig. 4.10B shows the degradation efficiency of atrazine with various catalysts. It was estimated according to the following equation:

$$Efficiency = \frac{c_0 - c}{c} \times 100\% \qquad (4.1)$$

where C_0 is the initial concentration of herbicide (ppm) and C is the concentration of herbicide after 18 minutes of irradiation. From Fig. 4.10B we can observe that the efficiency with 1% Ag in WO_3/SBA-15, the degradation efficiency has gone as high as 70 %. In addition, the stability of Ag-WO_3/SBA-15 composites was investigated under visible light irradiation by recycling experiments.

4.7 Mechanism for the degradation of Atrazine

Fig. 4.11 depicts of the mechanism of photocatalytic activity of Ag/ WO_3/SBA-15 composite in the process of the degradation of atrazine. SBA-15 is mesoporous with a uniform pore structure leading to absorb the relatively large amount of pollutant to build adsorption-desorption equilibrium in the dark. SBA-15 is found to be an ineffective photocatalyst in the process of the degradation of atrazine but it can serve as a good template to increase the effective surface area, which is vital for any photocatalytic process.

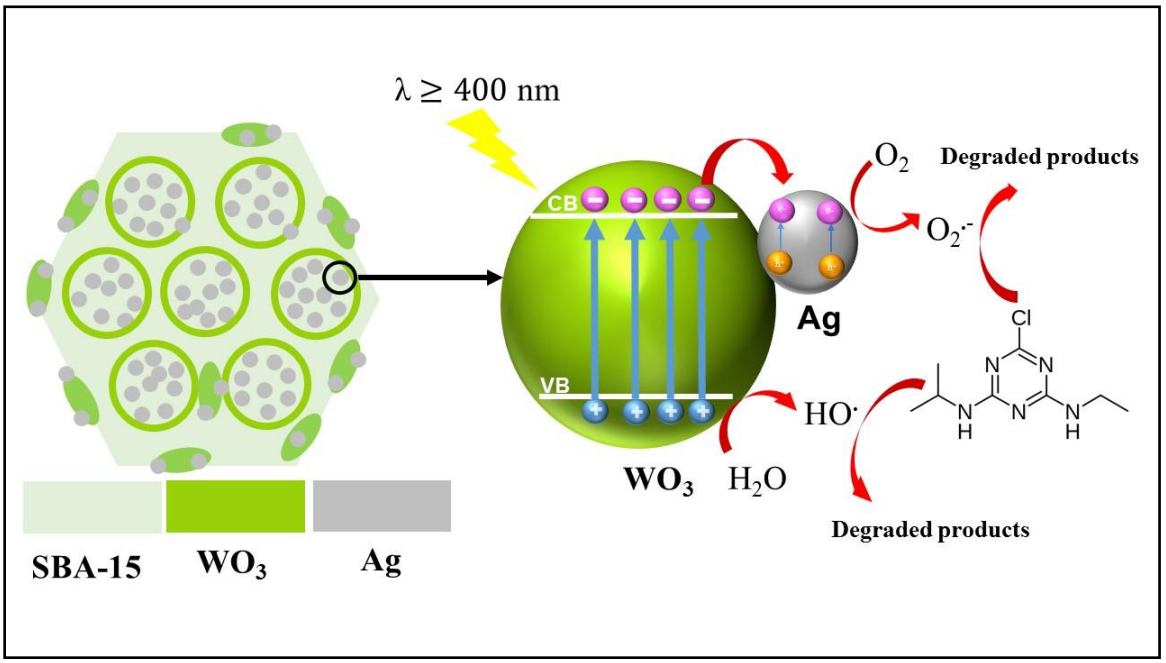

Figure 4.11: Proposed photocatalytic degradation process at the surface Ag-WO_3/SBA-15.

As we observed in the photocatalytic degradation of atrazine using WO_3/SBA-15, there exists an optimum balance between the surface area enhanced by the SBA-15 template and the content of WO_3 present in that template. When Ag is loaded to the WO_3/SBA-15 composite, a metal-semiconductor Schotky barrier is formed, where the electronic transport process of WO_3/SBA-15 composite is governed by the work functions Ag and WO_3 until the equilibrium is attained to form a new Fermi energy level[72]. In our case, the work function of Ag (4.7 eV) is smaller than that of WO_3 (5.7 eV)[83] and hence naturally, the electrons will transfer from silver to the conduction band of WO_3 to accomplish the Fermi level equilibration. Therefore, the surface of the WO_3 accumulates an excess of electrons, while the Ag accumulates positive charge leading to the spatial separation of charge carriers. This spatial charge separation due to the formation of Schotky barrier inhibits the electron-hole recombination which made the charge carriers available for the photocatalytic process and thereby increased the photocatalytic activity of Ag/WO_3/SBA-15 catalyst[70,84]. This reduced recombination of charge carriers is reflected on the reduced photoluminescence signal observed in Fig. 4.9. The photogenerated electrons reduce the adsorbed oxygen on the surface of the catalyst and produce super oxygen anionic free radical $O_2^{\bullet-}$. Then $O_2^{\bullet-}$ react with water to produce hydroxide radicals which further react with atrazine to give byproduct and water[84].

4.8 Summary

In this study, a wet impregnation method was employed to synthesize highly ordered mesoporous Ag-WO_3/SBA-15 heterogeneous catalysts with a well-dispersed metal oxide. The presence of WO_3 particles in SBA-15 pore channels assists in the uniform and

homogeneous dispersion of Ag particles and their synergic effect impose a significant impact in enhancing the photocatalytic performance of Ag-WO_3/SBA-15 nanocomposite. The high mesoporous surface area and open pore channel of SBA-15 framework matrix ensure dispersibility and accessibility of guest NPs and promote the transportation and diffusion of atrazine molecules. Also, loading of silver into the WO_3/SBA-15 promotes this material to be active in the visible spectral region and significantly reduced the electron-hole recombination. Catalytic degradation studies for advanced oxidation processes (AOPs) demonstrate that under optimum conditions the Ag-WO_3/SBA-15 catalysts can efficiently degrade 70% of atrazine in 18 min of visible light irradiation and can retain high stability and reusability. Therefore, mesoporous heterogeneous Ag-WO_3/SBA-15 catalysts can be considered as prospective candidates for AOPs in wastewater treatment.

CHAPTER 5

Visible-light-induced heterogeneous Photocatalytic degradation of methylparaben using Ag/AgBr@m-WO_3

5.1 Introduction

Application of heterogeneous photocatalysis in water treatment has been increasingly popular, due to its inherent simplicity, low operational cost, mild experimental conditions (temperature and pressure) and complete mineralization of the pollutants without any residual secondary pollution. Ever since, Fujishima and Honda[8] reported water splitting using TiO_2 electrode, many pure, doped and composite variants of TiO_2 have been synthesized and used for various photocatalytic and solar energy applications due to many positive attributes of TiO_2, like low cost, physical and chemical stability and high efficiency. However, one of the major constraints of TiO_2 as a photocatalyst is its wide band gap energy, that limits its activity in the visible spectral region and hence it cannot be a good photocatalyst that can be used to harness the abundant solar radiation. Also TiO_2, in particular shows low adsorption on the hydrophobic contaminants when used as photocatalyst for the purification of water. In addition to numerous variants of doped and composite TiO_2, many other semiconductor photocatalysts like CdS, SnO_2, WO_3, SiO_2, ZnO, Nb_2O_3, Fe_2O_3 have been used for various photocatalytic applications.

The nanostructured WO_3 has been proven to be an excellent visible-light-responsive photocatalyst due to its narrow band gap energy (between 2.4 and 2.8 eV), in addition to its stable physicochemical properties, and resistance to photo corrosions[85,86]. However,

the inherent band edges of WO_3 are not compatible with the oxidation and reduction potential, that favors the chemical reactions that lead to the elimination of organic substances from water. In order to overcome this problem, and at the same time harnessing other positive attributes of WO_3, many metals loaded WO_3 like Pd/WO_3[87], Pt/WO_3[88,89] and its composite forms like CuO/WO_3[90] and $CaFe_2O_4/WO_3$[91] were used as a photocatalyst for the removal of organic contaminants from water.

It is well-known that due to surface plasmonic resonance (SPR) effect, the noble metal (Au and Ag) doped semiconductor materials exhibit a significant enhancement of light absorption in the wide spectral range and this breakthrough opened up a new field of plasmonic photo-catalysis[92–94]. In SPR, when the incident light radiation of appropriate wavelength falls on the metal surface, the coherent oscillations of electrons in the noble metal set in, and the interaction between these electronic oscillations with the incident light promotes the light absorption due to resonance effect. Another advantage of plasmonic photocatalysis is the enhancement of the desired charge separation, promoted by the formation of Schottky junction between the metal and semiconductor and the internal electric field in the junction[95,74]. Another positive feature that can be used for photocatalysis is the mesoporosity of the material and many metal oxides semiconductors with ordered mesoporous structures have shown increased photocatalytic activity in many applications[96,97]. This is due to the increased specific surface area in the mesoporous materials and its positive effect on the creation of more active sites and the enhancement of the adsorption of reactant molecules on the semiconductor surface[98]. Also, ordered mesoporous channels promote quick intraparticle molecular charge transfer, and thereby prolong the lifetime of the separated electron-hole pairs by impeding their recombination,

which also further helps the improvement of photocatalytic activity [99,100,101]. Ordered mesoporous WO_3 has been extensively used for gas sensing application, due to its increased affinity with gas molecules, due to increased surface area, but only a few studies have been performed for photocatalytic applications[102–105].

The enhancement of the photocatalytic activity due to the increased visible light absorption brought about by the surface plasmonic effect led to the applications of many silver/ silver halide (Ag/AgX, X= Cl, Br, I) nanomaterials for the photocatalytic degradation of organic pollutants. In this line, silver bromide (AgBr) as such, is proven to be an excellent photoactive material, as it readily generates electron-hole pair when the visible radiation falls on it. The photo-generated electrons combine with interstitial silver ions to form silver atom and this makes AgBr quite unstable in its pure crystal structure[106]. The following chemical equations explain the above process:

$$AgBr + h\nu \rightarrow AgBr\ (h^+ + e^-) \quad (5.1)$$

$$e^- + Ag \rightarrow Ag_0^i\ (Ag^+ : interstitial\ silver\ ions) \quad (5.2)$$

$$AgBr \rightarrow Ag^+ + Br_2 \quad (5.3)$$

However, many reports have confirmed that the stability of AgBr can be improved and the consequent enhancement of photocatalytic activity can be achieved by dispersing it with certain support materials like in the form of composite materials like Ag/AgCl/WO_3[84], Ag@AgBr/Bi_2WO_6[107], Ag@AgBr/g-C_3N_4[108], Ag–AgBr@hierarchical hollow silica spheres (Ag–AgBr@HHSS)[109], AgBr/WO_3[110] Ag/AgBr/$WO_3.3H_2O$[111], mesoporous Ag/WO_3[83], and Ag-WO_3/SBA-15[50], which were reported to have an excellent visible light photocatalytic activity for various applications. It was reported in

some studies that the deposition of a trace amount of silver on the surface of AgBr@m-WO_3 has affected the photocatalytic activity of AgBr@-m-WO_3[87,112].

In the present work, the mesoporous WO_3 was initially synthesized by sole-gel method and it was used as a support material for AgBr to form AgBr@m-WO_3 composite and subsequently, atomic Ag was introduced in the AgBr@m-WO_3 composite by photo-reduction to produce Ag/AgBr@m-WO_3 as a final product (Fig. 5.1).

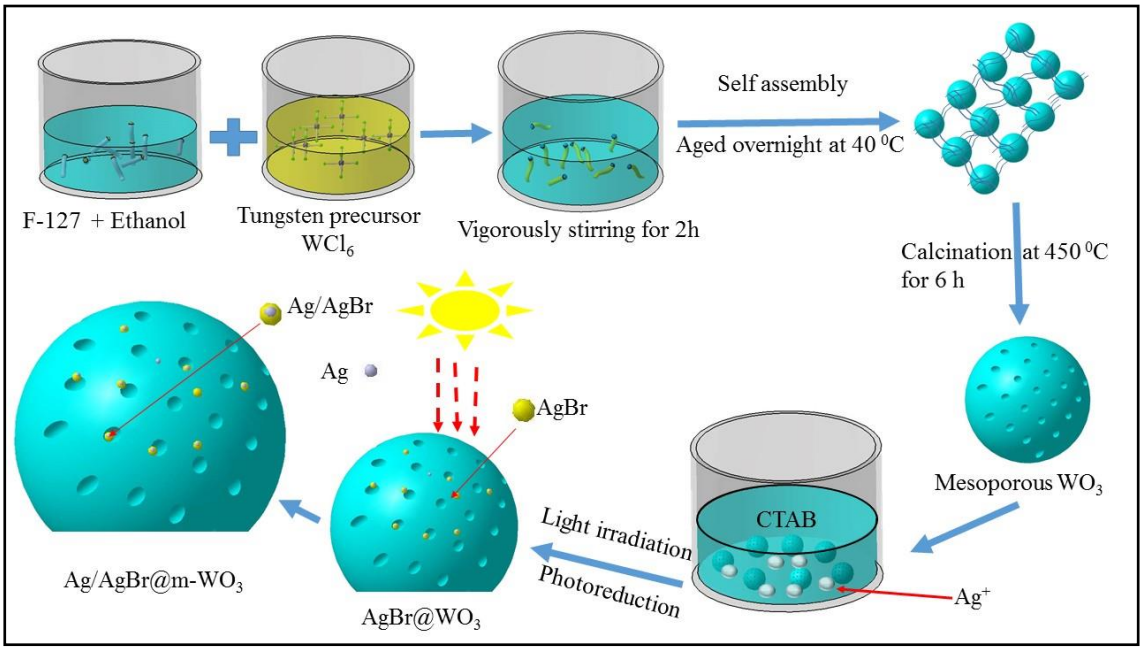

Figure 5.1: Schematic for the synthesis of Ag/AgBr@m-WO_3 photocatalyst.

The Ag/AgBr@m-WO_3 (with three different Ag content) were used as a photocatalyst under visible light radiation for the photocatalytic degradation of methylparaben in water and this photo-catalytic degradation was found to be quite substantial. Paraben has been used as preservatives in personal care products, pharmaceutical, cosmetic, and food stuff for a long time, due to their ability to prevent bacterial and fungal growth. Although parabens have been extensively used in most of the lifestyle products, the recent studies

have shown that they have some adverse health effect by disrupting the endocrine system by mimicking certain hormones in the body. Particularly, parabens mimic the activity of estrogen in the body cell, which is largely associated with breast cancer. Also, there are a few reports about the ecotoxicity of trace level of paraben in water (in ng/L to µg/L level), particularly about its adverse effects on various microorganism due to continuous discharge into the aquatic environment[113,114]. Parabens are considered as "pseudo-persistent" pollutants as a result of their continuous ejection into the water bodies and this became a cause for eco-toxicological concerns[115–117].

The motivations to use Ag/AgBr@m-WO_3 as photocatalyst for this photocatalytic removal process are (i) the enhancement of visible absorption due to surface plasmonic effect brought about by the introduction of atomic Ag (ii) the reduction of charge recombination due to the formation of metal-semiconductor Schottky junction and also the presence of mesoporosity in WO_3 and (iii) the enhancement of active sites due to the increased surface area due mesoporosity. Morphological and optical characterizations of the synthesized Ag/AgBr@m-WO_3 were also carried out to explain the observed enhancement in the photocatalytic removal of methylparaben in water.

5.2 Experimental

5.2.1 Chemicals and materials

Pluronic P127 (Sigma-Aldrich), Tungsten (VI) chloride WCl_6. Silver nitrate ($AgNO_3$, Sigma-Aldrich, 99%), cetyltrimethylammonium bromide (CTAB).

5.2.2 Synthesis of mesoporous WO_3 catalyst

A measure of 1.0 g of Pluronic P-127 (Sigma-Aldrich) was dissolved in 18 ml of ethanol by stirring it for 30 minutes at room temperature and to this solution, 0.01 mol of WCl_6 (Sigma-Aldrich) was added and was vigorously stirred for 2 hours. The resulting sol solution was allowed to gel in an open Petri dish at 40 ℃ for 5 days and during this process, WCl_6 hydrolyzes and polymerizes into a tungsten oxide network. In order to remove the surfactant species, the bulk sample, prepared above was calcined at 450℃ for 6 hours in air at the rate of 2.0 ºC/ minute.

5.2.3 Synthesis of Ag/AgBr@m-WO_3

A measure of 0.25 g of m-WO_3 (prepared as above) and 0.12 g of Cetyltrimethylammonium bromide (CTAB) (Sigma-Aldrich) were added into 100 ml of distilled water and after stirring the mixture for 30 minutes at room temperature, 1.0 ml of $AgNO_3$ (0.1008M) was added and stirred for further 20 minutes. Subsequently, the above product was irradiated using visible light from a solar simulator (150 W xenon lamp) for different duration in order to produce catalysts with different contents of Ag through the photoreduction of Ag^+ ions in AgBr into Ag^0 NPs. The catalyst was washed with distilled water, dried at 80 ℃ for 24 hours in the dark and finally, calcined in air at 300 ℃ for 3 hours to obtain the Ag/AgBr@m-WO_3 catalyst with different contents of metallic Ag^0 NPs in it.

5.2.4 Material Characterization

The phase and crystallinity of the synthesized materials were investigated by XRD (Siemens D5005) equipped with Cu anode and variable slits. The morphology and the microstructure of the synthesized materials were studied by scanning electron microscopy (SEM), Energy dispersive spectroscopy (EDX) and high-resolution transmission electron microscopy (HR-TEM) (JEM2100F, JEOL, operated at 200 KV). The diffuse reflectance spectra (DRS) were taken using a Shimadzu (UV-2450) UV-Visible spectrophotometer, where the BaSO4 fine powder was used as a standard for the baseline and the spectra were recorded in the 200 to 800 nm wavelength range. Micromeritics Tristar 3000 system was used to measure N_2 adsorption/desorption isotherms of the samples. The system is equipped with dedicated software which uses conventional analysis such as Brunauer-Emmett-Teller (BET) and Barrett-Joyner-Halanda (BJH) method for the determination of pore size distribution. Prior to the measurement, the samples were degassed for 4 h at 300 °C for the composites.

The phase and crystallinity of the synthesized materials were investigated by XRD (Siemens D5005) equipped with Cu anode and variable slits. The diffuse reflectance spectra (DRS) were taken using a Shimadzu (UV-2450) UV-Visible spectrophotometer, where the $BaSO_4$ fine powder was used as a standard for the baseline and the spectra were recorded in the 200 to 800 nm wavelength range. A Micromeritics Tristar 3000 system was used to measure the N_2 adsorption/desorption isotherms of the samples. Prior to the measurement, the samples were degassed for 4 h at 300 °C for the composites. The surface area was calculated using the Brunauer-Emmett-Teller (BET) equation and the pore volume was calculated from $P/P_o \sim 0.95$.

5.3 Photocatalytic degradation of methylparaben under visible light

For the study of the photocatalytic degradation of methylparaben, 25 ml of 10 ppm methylparaben solution and 25 mg catalyst were taken in a beaker and the suspension was magnetically stirred for 15 min in the dark to establish the adsorption-desorption equilibrium of methylparaben at the surface of the catalyst. A sample was removed after the equilibration period and constituted time zero. The suspension was irradiated at room temperature with a broadband of light source (450 W Xe arc lamp) equipped with the neutral density optical filter to allow the wavelength of light above to 400 nm, and aliquots were removed at regular time intervals, centrifuged at 13,500 rpm for 5 minutes and the suspension was filtered with 0.22 µm filter to remove any catalyst particles in the test solution. The concentration of methylparaben in the samples was quantified using a high-performance liquid chromatograph (HPLC, (Prominence Modular HPLC, Shimadzu Corporation, Japan) equipped with a photodiode array detector. A C18 column (250 x 4.6 mm, particle size 5 µm) was employed. The elution phase is the mixture of methanol/water (70:30, v/v) phase at a flow rate of 1.0 mL/min and the injection volume was 20 µL. The retention time of methylparaben under these conditions was 4.0 min. For scavenger studies, 1.0 mM of EDTA, isopropyl alcohol (IPA) and 1,4-benzoquinone (BQ) were prepared for mechanistic studies for the holes (h_{vb}^{+}), hydroxide ($^{\bullet}OH$) and superoxide radicals ($O_2^{-\bullet}$) respectively.

5.4 Results and Discussion

5.4.1 Morphological Characterization

XRD of synthesized mesoporous WO_3 and the same loaded with Ag/AgBr having different contents of photoinduced Ag atoms (obtained by different irradiation time) are depicted Fig. 5.2. The XRD pattern for m-WO_3 (JAPDF 01-072-0677) is shown in Fig. 5.2a and the same for Ag/AgBr@m-WO_3 with different contents of metallic Ag^0 NPs are shown in Fig. 5.2 b-d. In Fig. 5.2, we can observe that in the presence of Ag/AgBr in m-WO_3, the intensities of m-WO_3 diffraction peaks diminished and the same time three new peaks at 31.0^o, 44.2^o and 72.2^o, due to the face centered cubic structure of AgBr (JAPDF: 06-0438) appeared. However, XRD result does not establish the existence of metallic Ag present in Ag/AgBr@m-WO_3, and the same was reported in the case of Ag/AgBr/TiO_2, AgBr/BiOBr and Ag/AgBr/WO_3 nanocomposites[118,119] and could be due to low amounts of the Ag^o nanoparticles and/or their small size.

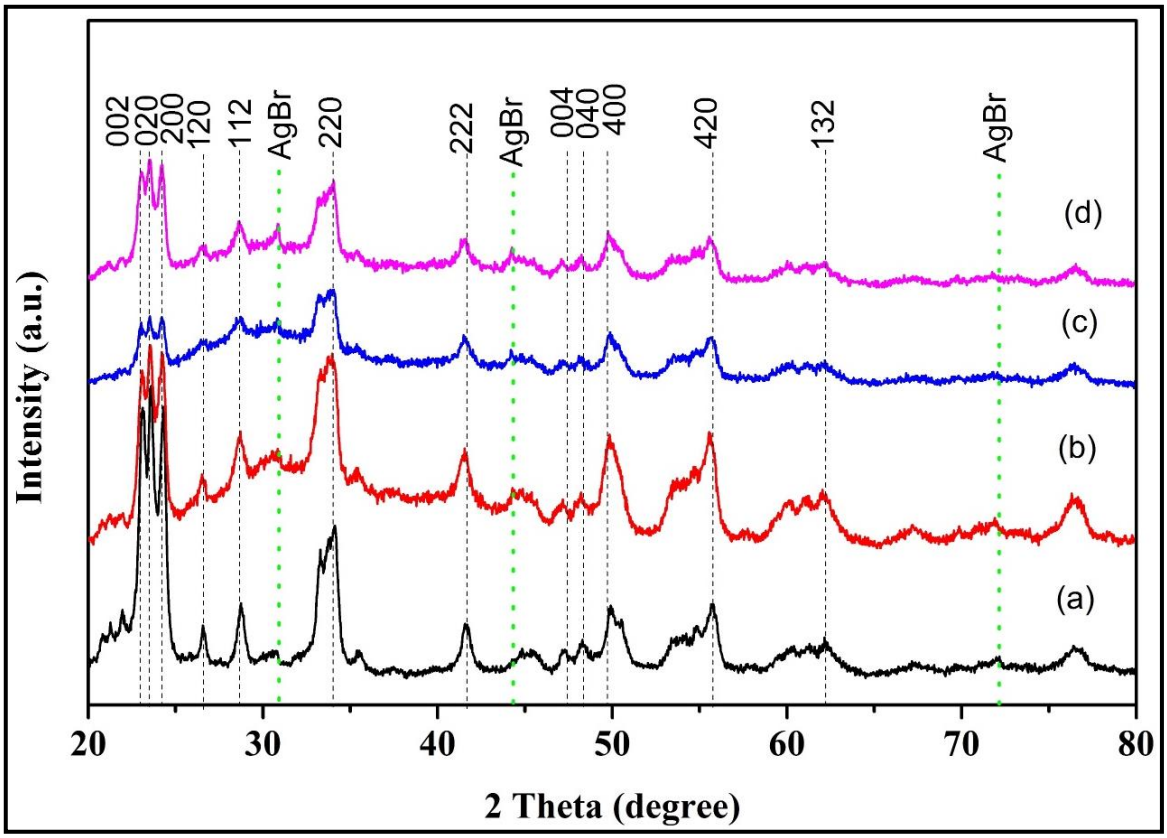

Figure 5.2: XRD patterns of (a) m-WO_3 (b) 15 min Ag/AgBr@m-WO_3 (c) 30 min Ag/AgBr@ m-WO_3 (d) 45 min Ag/AgBr@ m-WO_3.

High-magnification scanning electron microscopy (SEM) images were taken of m-WO_3 (Fig. 5.3a) and Ag/AgBr@m-WO_3 taken after 15 minutes of irradiation (Fig. 5.3b). The Ag/AgBr@m-WO_3 composite consists of spherical particles in the range of 20 - 40 nm. SEM images with higher resolution were not obtained as AgBr may get decomposed by the high-energy electron beam. SEM-EDX elemental mappings (Figs. 5.3c – 5.3f) confirm the presence of W, O, Br and Ag, respectively. On comparing Fig. 5.3(e) with 3(f), we can observe that the distribution of Ag is higher than that of Br. This is because Ag is present as Ag metal as well as AgBr on the surface of mesoporous WO_3. Fig. 5.3f also shows that the distribution of Ag particles is homogeneous.

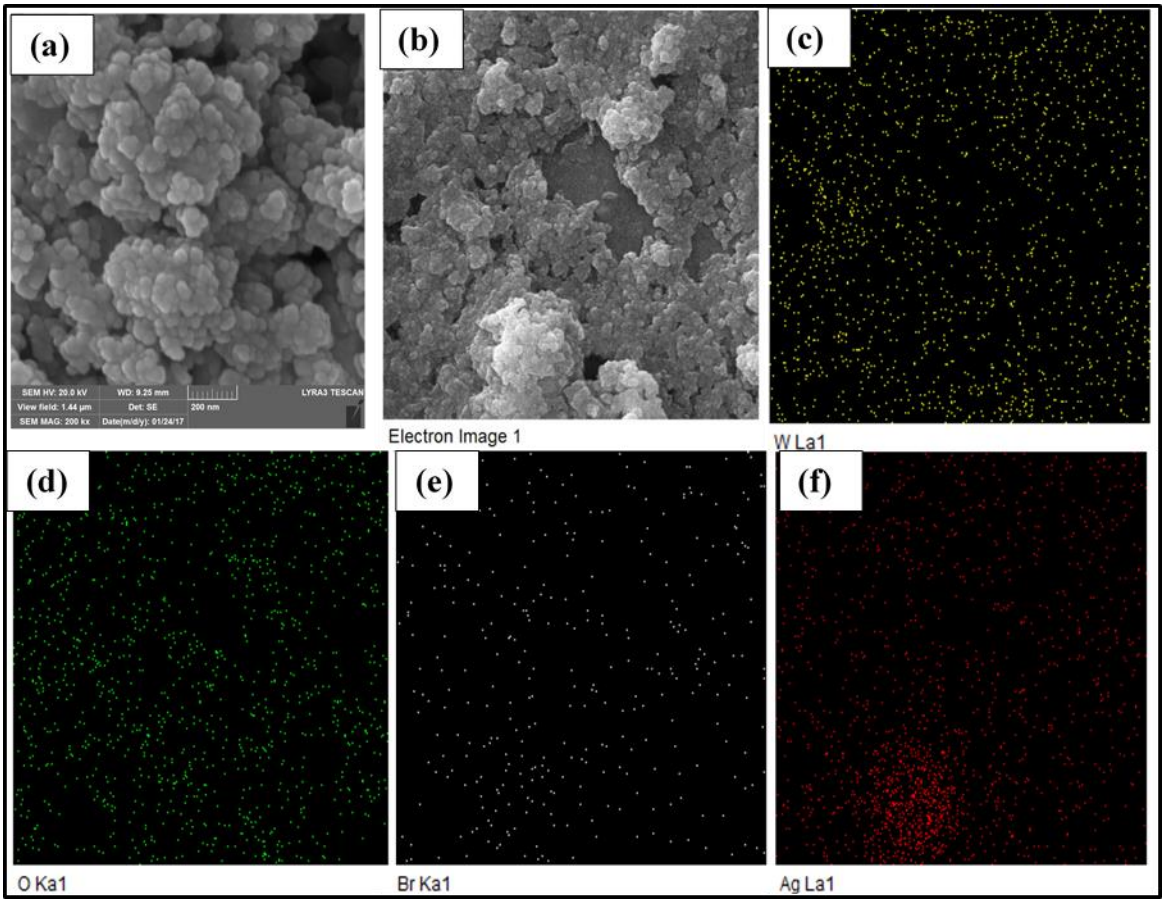

Figure 5.3: (a) High magnification SEM image of m-WO_3 particle, (b) SEM of 15 min Ag/AgBr@m-WO_3 (c) SEM-EDX elemental mapping image of W La1 on this area, (d) SEM-EDX elemental mapping image of O Ka1 on this area, (e) SEM-EDX elemental mapping image of Br Ka1 on this area.

The mesoporous structure of the catalyst was further studied by HR-TEM (Fig. 5.4). The TEM image of WO_3 shows rectangular plate-like structure (Fig. 5.4a) while the Ag/AgBr@m-WO_3 shows a combination of oval and spherical shapes (Fig. 5.4b). The particle sizes were in the range of 10 - 50 nm, which is still smaller than the values deduced from the SEM images.

The interplanar distances determined from the high-resolution image were found to be 0.362, 0.283 and 0.251 nm, which are consistent with the spacing's of m-WO_3 (200), AgBr (200)[84,120] and Ag (111) planes, respectively. This confirms the homogenous

distribution of Ag/AgBr nanoparticles on the surface of mesoporous WO_3. The specific surface areas and the pore volume in the range of (0.23 – 0.12) $x10^{-2}$ cm^3 g^{-1} for m-WO_3 and Ag/AgBr@m-WO_3 in which are summarized in Table 1. The surface areas are ~ 12 – 16 m^2/g and pore volumes are ~ 9.7 – 10.2 nm.

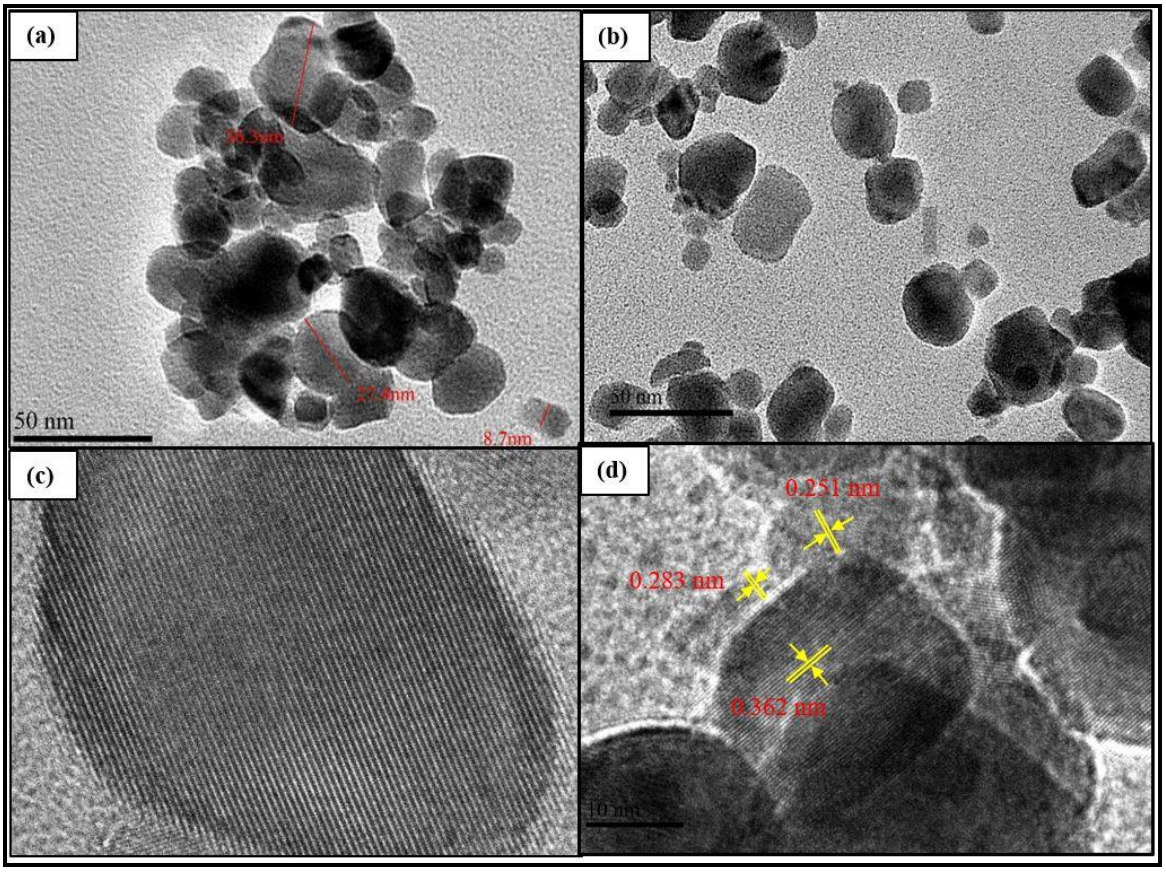

Figure 5.4: TEM images of high magnification photocatalyst (a) m@WO_3 (b) 15 min Ag/AgBr@m-WO_3 (c-d) d-spacing of m-WO_3 and 15 min Ag/AgBr@WO_3 respectively.

5.4.2 Optical Characterization

In order to eliminate the effect of light scattering by a particle in the absorption spectra, the diffuse reflectance spectra were transformed into Kubelka-Munk function[121–123]. From Fig. 5.5, it is quite clear that as compared to pure m-WO_3, Ag/AgBr@-m-WO_3 shows enhanced absorbance, particularly in the visible region of the spectrum. Moreover,

Ag/AgBr@-m-WO_3 with 30 minutes of irradiation has much stronger absorption in the visible region, compared to one with 15 minutes of irradiation. This indicates that Ag nanoparticles were effectively deposited into the photocatalyst composite and the SPR of Ag nanoparticles in Ag/AgBr@m-WO_3 is responsible for the enhancement of the visible light absorption[94]. Inset Fig. 5.5 shows the Tauc plots[81] for m-WO_3 and Ag/AgBr@m-WO_3. The band gap energies of the materials were determined and listed in Table1. The band gap energy of m-WO_3 is 2.6 eV, and giving allowance for the statistical error, the change of bandgap energy due to the introduction of Ag/AgBr is not appreciable.

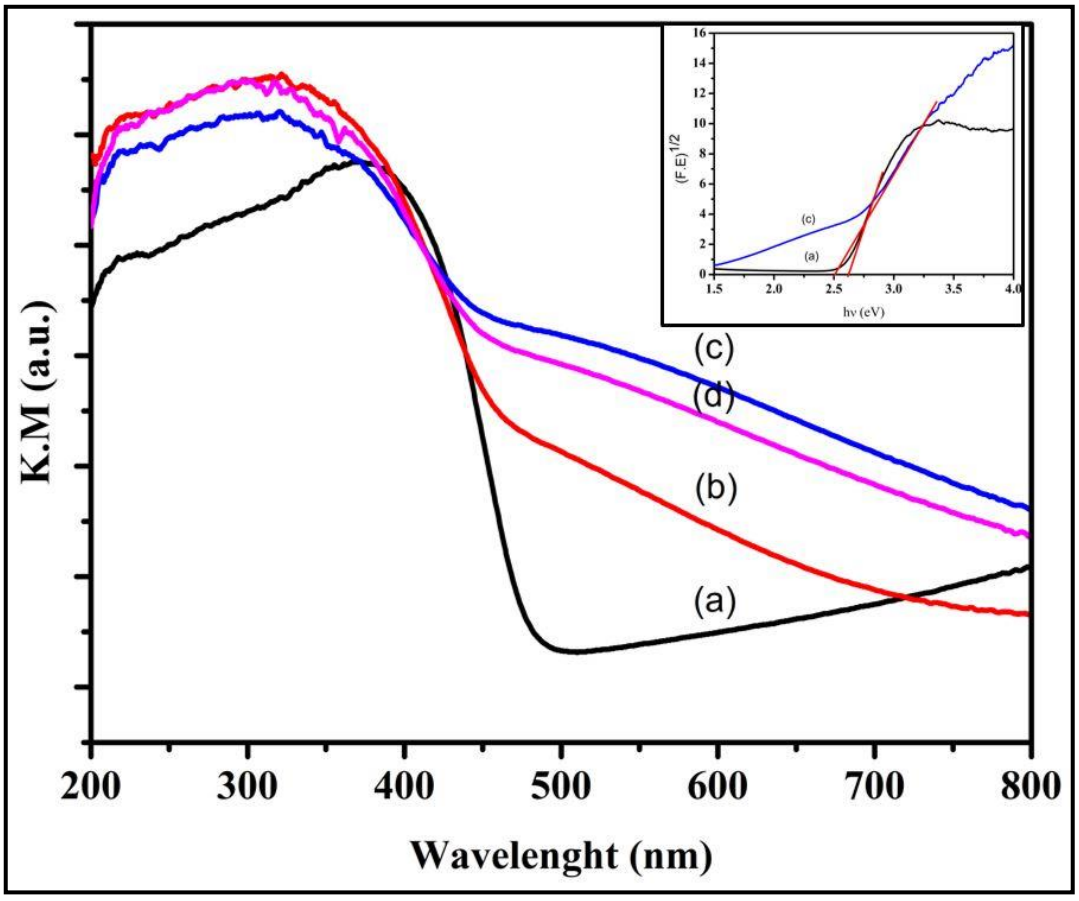

Figure 5.5: UV-VIS diffuse reflectance spectra represented as Kubelka-Munk Function for (a) m-WO_3 (b) 15 min Ag/AgBr@WO_3 (c) 30 min Ag/AgBr@WO_3 and (d) 45 min Ag/AgBr@WO_3 Inset shows the Tauc plots for m-WO_3 and 30 min Ag/AgBr@WO_3 in the order (a) and (c).

5.4.3 Photocatalytic degradation methylparaben

The Ag/AgBr@m-WO_3 composites with different contents of atomic Ag (due to different photo-reduction time during synthesis) and pure m-WO_3 were used as photocatalysts for the degradation of methylparaben in water under visible radiation of wavelength $\lambda \geq 400$ nm. As can be seen from Fig. 5.6, the photocatalytic degradation of methylparaben over m-WO_3 is not appreciable compared to the Ag/AgBr@m-WO_3 composites. Ag/AgBr@m-WO_3 with the photo- reduction time of 30 minutes (during synthesis) was the best performer with 85% degradation of methylparaben after 180 minutes under visible light radiation. This result indicates that the presence of Ag/AgBr plays a significant role in the photocatalytic degradation of methylparaben. The degradation rate of 30 min Ag/AgBr@m-WO_3 was three times faster than the m-WO_3. From the linear plots of $-\ln(C/C_o)$ vs irradiation time, it can be deduced that the photodegradation of methylparaben follows a pseudo-first order kinetics (Fig. 5.7). The rate constants for the photodegradation can be obtained from the slopes of linear plots and are listed in Table 4.2. The photocatalytic degradation of methylparaben in water can be ranked in the following order: 30 min Ag/AgBr@m-WO_3 > 45 min Ag/AgBr@m-WO_3 > 15 min Ag/AgBr@m-WO_3 > m-WO_3.

Table 5-1: BET surface area of different nanocomposite and rate constant methylparaben degradation of m-WO_3 and Ag/AgBr@WO_3 nanocomposites.

Samples	Surface area (m^2 g^{-1})	Vpx10^{-2} (cm^3 g^{-1})	Band gap (eV)	K (min^{-1})
m-WO_3	15	0.23	2.60	0.00161
15 min Ag/AgBr@WO_3	15	0.18	2.54	0.00253
30 min Ag/AgBr@WO_3	16	0.14	2.40	0.00981
45 min Ag/AgBr@WO_3	11	0.12	2.54	0.00377

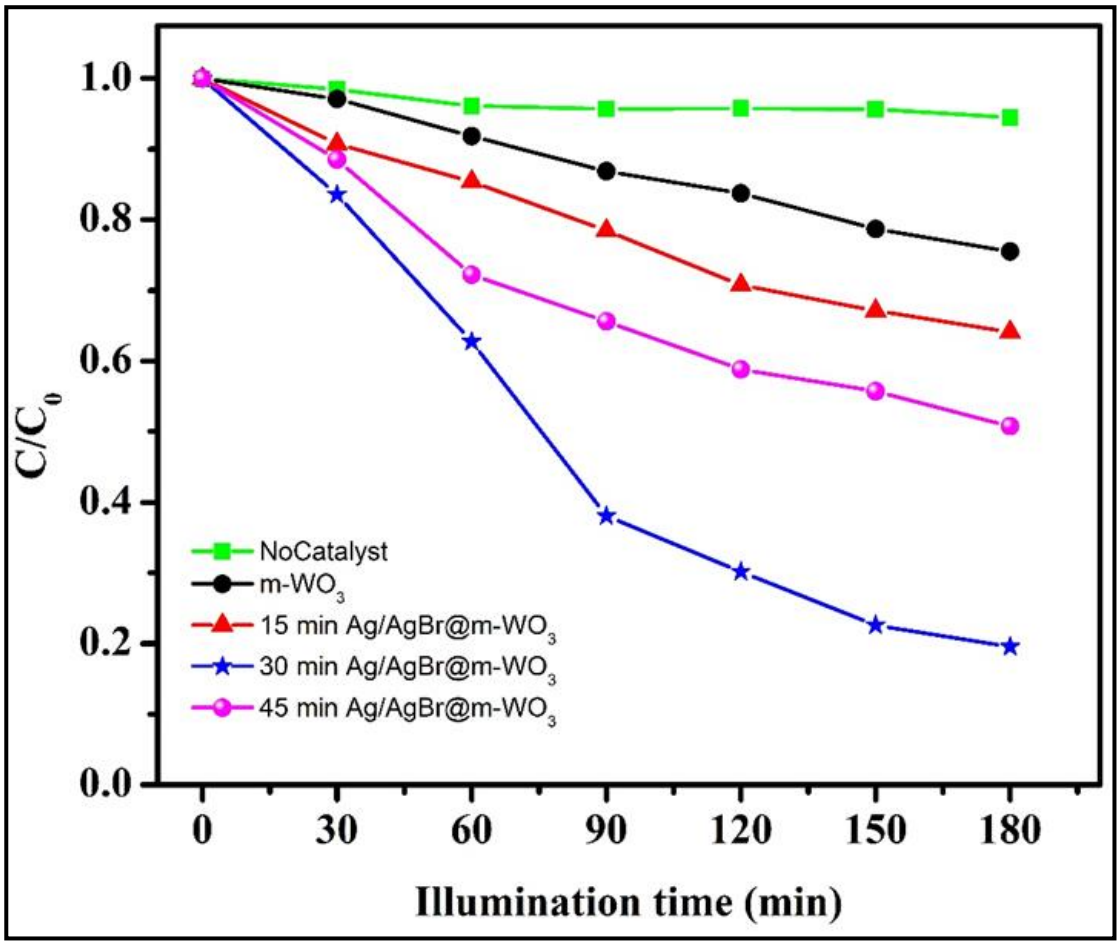

Figure 5.6: Photocatalytic degradation of methylparaben in aqueous suspension under visible light irradiation with different photocatalyst under visible light.

In Ag/AgBr@m-WO_3 with 15 minutes of photo-reduction (during synthesis) the content of atomic silver is smaller compared to Ag/AgBr@m-WO_3 with 30 minutes of photo-reduction. Consequently, the SPR effect is reduced which leads up to less visible light absorption (Fig. 5.7), and weaker photocatalytic degradation of methylparaben in water. On the other hand, when the Ag content in Ag/AgBr@m-WO_3 is beyond a certain limit, as for the sample with 45 minutes of photoreduction, a portion of the Ag nanoparticles become active sites that promote the undesirable electron-hole recombination and consequently the photocatalytic activity is diminished. Also, a higher content of AgBr in m-WO_3 will lead to the formation of nanoclusters of Ag/AgBr species, which reduces the active sites on the surface of m-WO_3 through agglomeration of the particles[124,125]. The weight % of AgBr on 15 min, 30 min and 45 min of Ag/AgBr@m-WO_3 catalyst was 0.65 %, 0.81% and 1.0 % AgBr respectively.

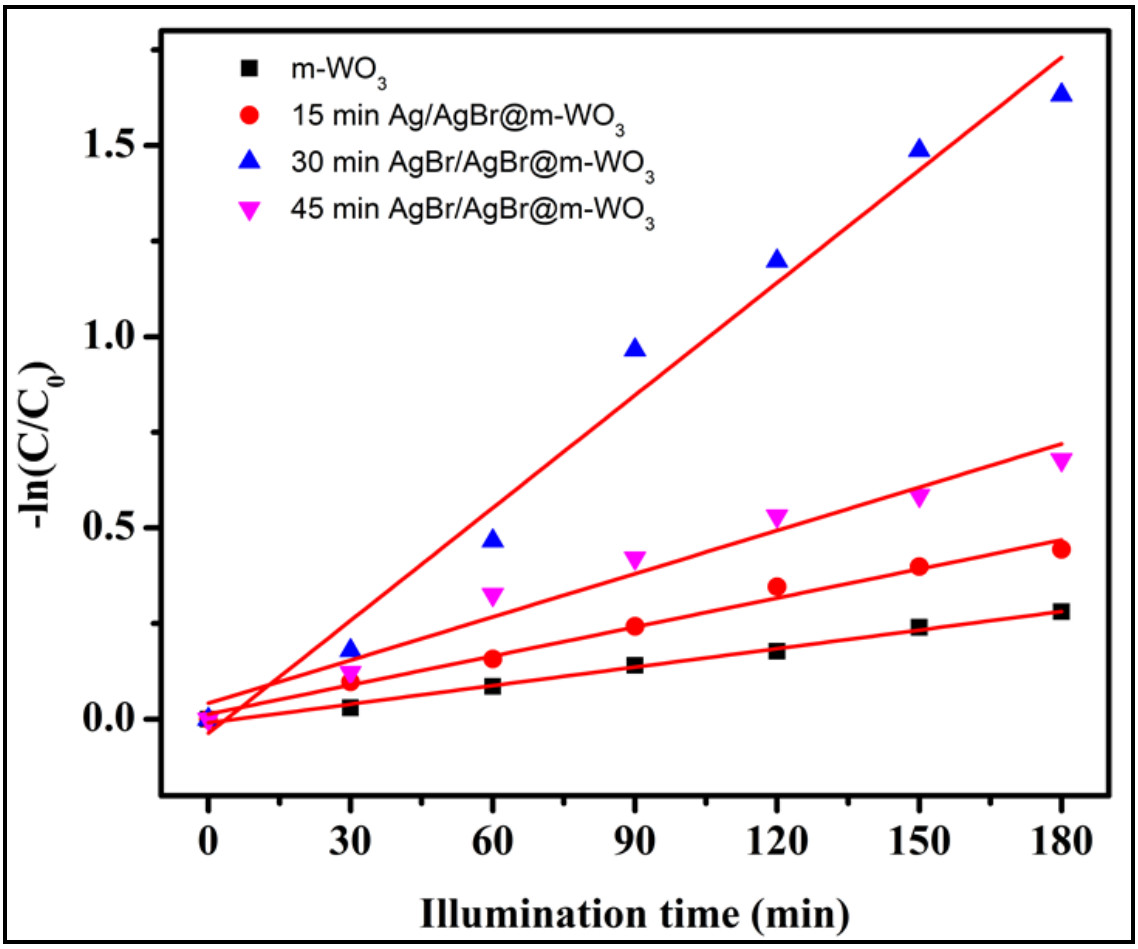

Figure 5.7: Plots of $-\ln(C/C_0)$ vs. irradiation time for the photocatalytic degradation of methylparaben with different photocatalysts under visible light.

In addition to the photocatalytic activity, the stability and the reusability of Ag/AgBr@m-WO_3 were investigated (Fig. 5.8). The photoactivity of the catalyst remained quite stable even after five cycles of use.

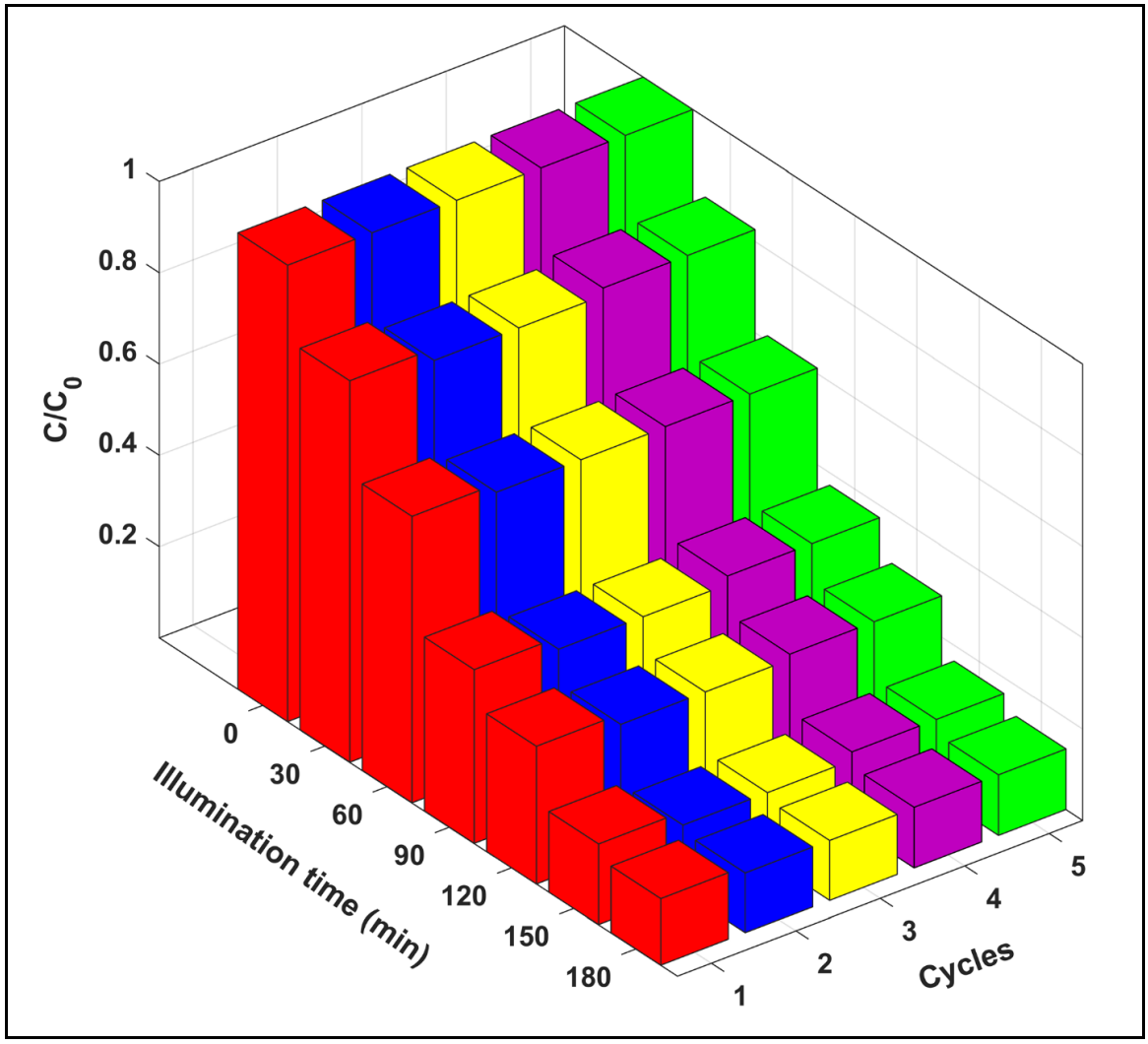

Figure 5.8: The reusability of the photocatalyst for 30 min Ag/AgBr@m-WO_3.

The degradation rate of 30 min Ag/AgBr@m-WO_3 was three times faster than the m-WO_3. Th degradation rate follows pseudo-first order reaction which indicates that the ratio Ag and AgBr were significant parameters on the rate of photodegradation. In order to quantify the photocatalytic degradation of methylparaben in water with three different

variants of Ag/AgBr@m-WO_3, we transformed the photocatalytic degradation curves in Fig. 5.6 in a linear form (-ln (C/C_0) vs. irradiation time) and are shown in Fig. 5.7 The photocatalytic degradation of methylparaben follows the pseudo-first-order kinetic model and the slopes of the above linear graphs represent the photocatalytic degradation rate constants, which are listed in Table 5.2 for all the catalysts used in this work. The photocatalytic degradation rate constant for methylparaben with of 30 min Ag/AgBr@m-WO_3 is 0.00991 min^{-1}, which is much higher than the same with m-WO_3. In addition to the photocatalytic activity, we examined the stability and the reusability of Ag/AgBr@m-WO_3 and the results are summarized in Fig. 5.9, which shows that all the catalysts are quite stable even after five cycles of use with the photocatalytic reaction time of 5 times for each cycle. In addition to the photocatalytic activity, the stability and the reusability of Ag/AgBr@m-WO_3 were investigated. The photoactivity of the catalyst remained quite stable even after five cycles of use.

5.5 Mechanism of Methylparaben degradation

5.5.1 Free radical and holes scavenging experiments

To understands the interaction between Ag/AgBr and mesoporous WO_3 and the active species generated during the photocatalyzed degradation of methylparaben using m-WO_3 and Ag/AgBr@m-WO_3, we carried out holes (h_{vb}^+) scavenging and free radical experiments. In this part of the study, EDTA, Isopropyl alcohol (IPA) and 1,4-benzoquinone (BQ) are respectively used as holes (h_{vb}^+) scavenger, hydroxyl radical scavenger ($^{\bullet}OH$), superoxide radical scavenger ($O_2^{\bullet-}$)[85,86]. As it is clear from Fig. 5.9, isopropyl propyl alcohol ($^{\bullet}OH$ scavenger) does not bring about any change in the

photocatalytic degradation of methylparaben, while BQ ($O_2^{\bullet-}$ scavenger) and EDTA (hole scavenger) decrease the catalytic activity[87,88]. Generally, more the role of the reactive species, more reduced is the photoactivity and on this basis, our results indicate that the $^{\bullet}OH$ radical has no active role and $O_2^{\bullet-}$ was the main active species in the degradation of methylparaben. However, it was noticed that the suppression of BQ is not so high, which indicates the possible role of another active species. Knowing that the holes mostly accumulate on the valance band of AgBr and it can oxidized bromide ion to bromine Br_2 atoms, which function as a reactive species to degrade methylparaben[126,127]. This explains the minor effect of the holes in the degradation of methylparaben.

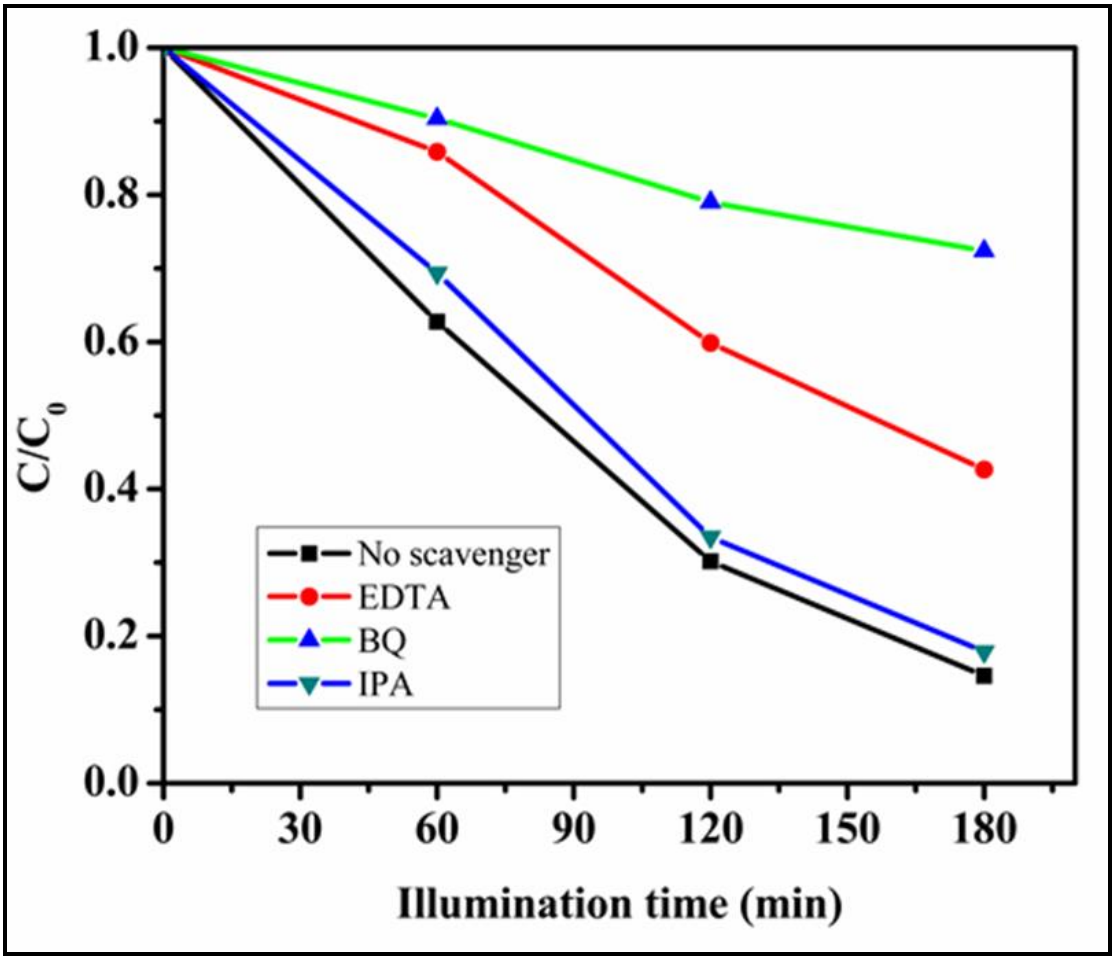

Figure 5.9: Effect of different scavenger on the photocatalytic degradation in the presence of 30 min Ag/AgBr@m-WO_3.

5.5.2 Charge transfer mechanism

Fig. 5.10 describes the proposed charge transfer mechanism for the photodegradation of methylparaben over the Ag/AgBr@m-WO_3 composite catalyst. When Ag/AgBr@m-WO_3 is irradiated with visible light, photoexcited electron-hole pairs are generated in AgBr, m-WO_3 and Plasmon excited Ag NPs. The photo-generated electrons from Ag NPs migrate to the conduction band of WO_3 and convert O_2 adsorbed on WO_3 to $O_2^{\bullet-}$ and at the same time, the photo-generated holes are trapped by AgBr particles due to surface Plasmon state of silver NPs [128] and this mechanism results in the efficient charge separation. Another charge separation is mediated by the migration of photogenerated electron into the metallic silver on the surface of WO_3[129] and at the same time, holes from AgBr oxidizing Br^- to Br^0. In addition to these charge transfer mechanism, methylparaben can directly be oxidized by the plasmon-induced h^+ (or Ag^+) on the silver NPs, and this also accelerates the process of transforming photo-oxidized Ag NPs back to their initial state. Mesoporous WO_3 provides more adsorption active sites for pollutant due to the higher specific surface area.

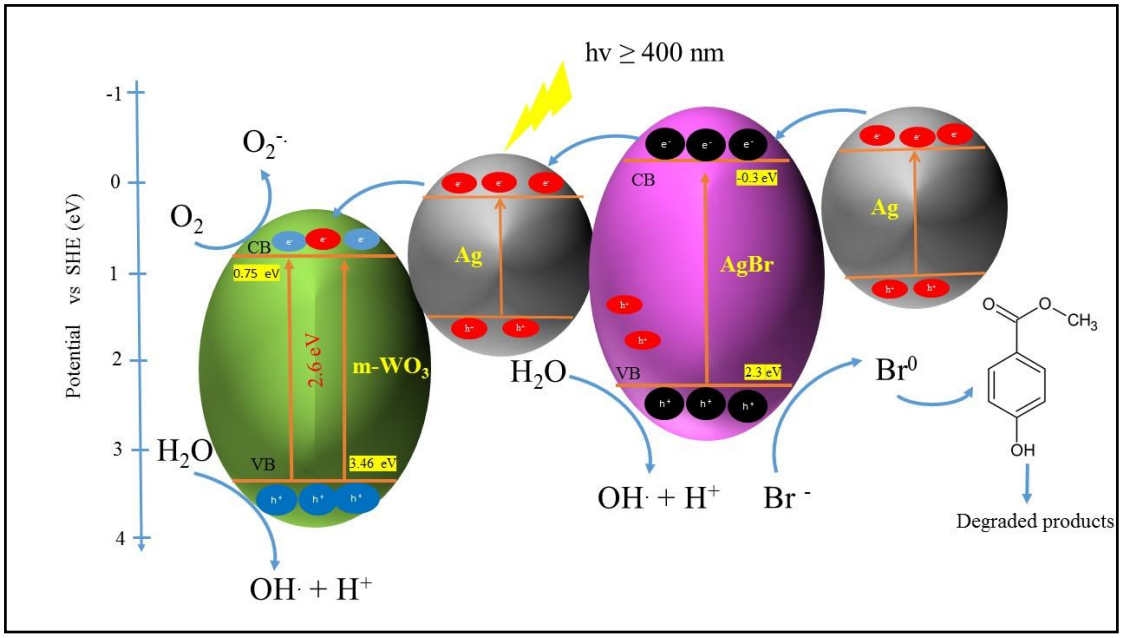

Figure 5.10: Schematic for the mechanism of photocatalytic degradation of methylparaben with Ag/AgBr@m-WO_3 under visible light.

5.5.3 Major by-products of methylparaben and reaction pathway

To characterize photocatalytic by-products of this reaction, experiments were carried out at ambient conditions (1.0 mg L^{-1} of Ag/AgBr@m-WO_3 as photocatalyst) using the stock solution of methylparaben (10 mg L^{-1}) in the presence of solar radiation in the visible spectral region. Samples were withdrawn for analysis after 180 and 240 minutes of irradiation and were analyzed by LC-MS to identify the intermediates, which are shown in Fig. 5.11

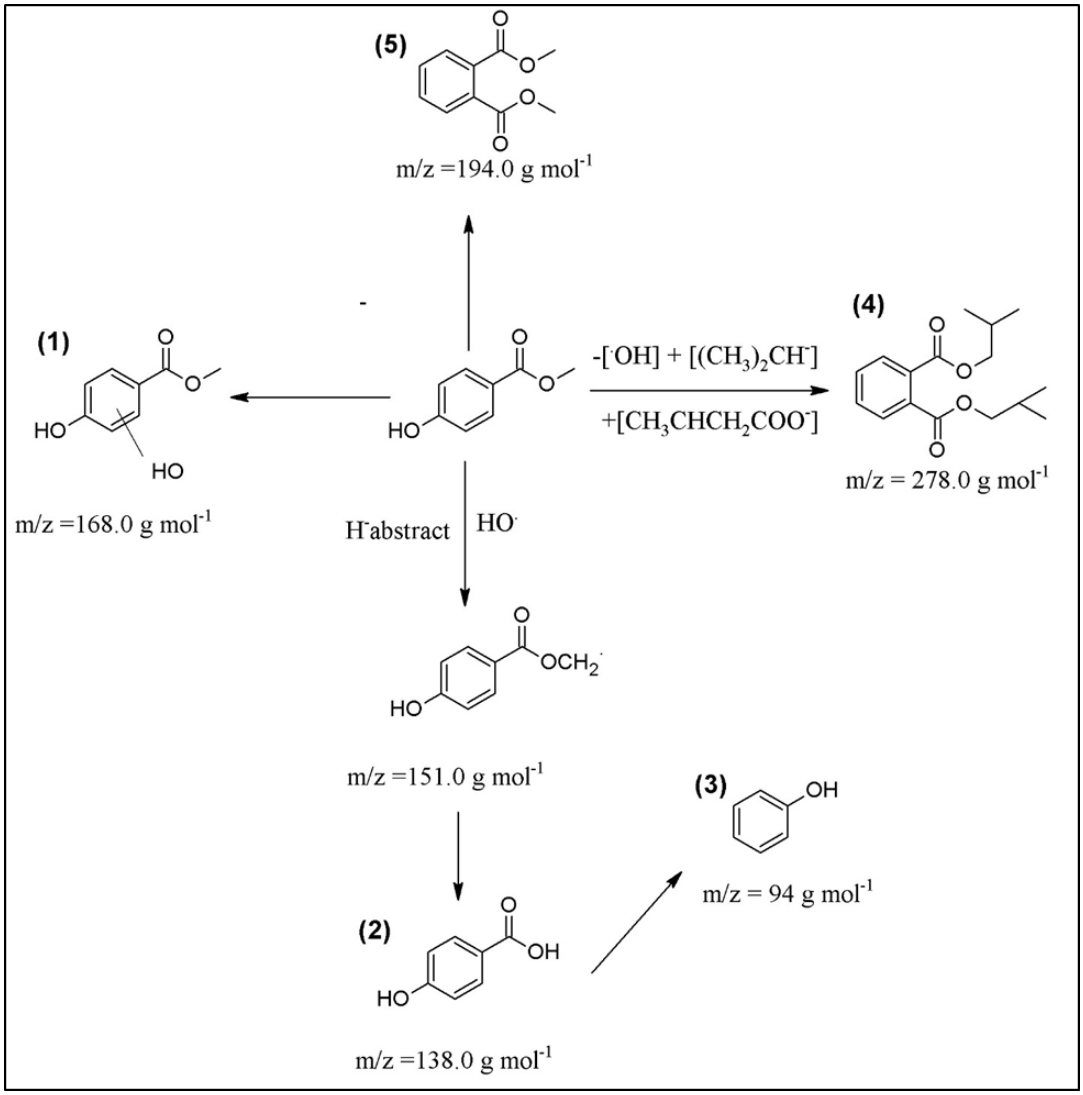

Figure 5.11: The photocatalytic reaction mechanism for the degradation of methylparaben.

In the current study, an effort was made to explain the mechanism and reaction pathways through the by-products identification, formed during the photocatalytic treatment procedure of methylparaben. Fig. 5.11 shows the suggested chemical formula and the value of detected ion exact mass for identified products of the degradation, during the methylparaben photocatalytic degradation process. Overall, five of the by-products was tentatively identified from the screening of the treated samples, followed by the reaction pathway of the methylparaben degradation in analyzed samples.

As T. Velegraki et al[130] reported the methylparaben degradation proceed by three different ways: (i) hydroxide radical attack on the methylparaben, (ii) the reaction of methylparaben with photo-generated hole generated in WO_3 and (iii) direct oxidation of methylparaben by dissolved oxygen in the water. During the treatment, the methylparaben toxicity or at least part of it remains in the solution because most of the by-products of methylparaben contain the core structure of the compound.

When the hydroxide radical attacked methylparaben at methyl group and hydrogen in the aromatic ring to produce 4-hydroxybenzoic acid **(1)** and **(2)** dihydroxybenzoic acid. Also, the last product is further oxide to phenol **(3)**. The formation of 1,2-benzenedicarboxylic acid bis-(2 methylpropyl) ester **(4)** and benzendicarboxylic acid **(5)** could be attributed to coupling at high concentration [53]. Furthermore, the formation of **(4)** and **(5)** could be attributed to the addition of 3-methylbutanoic acid group at the aromatic ring at C-2 and the di-hydroxylation and consequently addition of isobutene and methyl moieties at methyl acetate group, respectively.

5.6 Summary

In this study, highly ordered mesoporous WO_3 was synthesized by sol-gel method and subsequently, deposition-precipitation method was employed to synthesize AgBr@m-WO_3. Different levels of atomic silver were generated on the surface of AgBr@m-WO_3 by photoreduction method to get Ag@AgBr-m-WO_3. The synthesized material was used as a photocatalyst for the degradation of methylparaben in water. It was observed that the presence of Ag/AgBr on the surface of m-WO_3 brought about a significant enhancement in the photocatalytic performance of Ag/AgBr@m-WO_3 nanocomposite. The

enhancement of photocatalytic degradation can be attributed to the surface plasmonic effect due to atomic Ag and consequent enhancement of visible absorption, the reduced of charge recombination due to the formation of metal-semiconductor Schottky junction and the enhancement of surface area due to mesoporosity. Morphological and optical characterizations of the synthesized Ag/AgBr@m-WO_3 were also carried out to explain the efficiency of this photocatalytic material in the process of removal of methylparaben in water.

CHAPTER 6

Conclusion and recommendations

6.1 Conclusion

In this thesis, we have developed several WO_3 based visible light driven photocatalyst for degradation of persistent organic such as herbicide and pharmaceutical compound in a water sample. These photocatalysts can absorb visible light, stable and nontoxic under visible light irradiation. In all the cases, the separation of the catalyst from the water can be easy.

In this study, the Ag/WO_3/SBA-15 nanocomposite, the intimately the Ag disturbed homogenously between WO_3 and SBA-15, as well as relatively high surface SBA-15, the high mesoporous surface area and open pore channel of SBA-15 framework matrix ensure dispersibility and accessibility of guest NPs and promote the transportation and diffusion of atrazine molecules. Also, loading of silver into the WO_3/SBA-15 promotes this material to be active in the visible spectral region and significantly reduced the electron-hole recombination which enhanced the efficiency of separating the photo-generated charge carriers, resulting in high activity, with approximately 80% degradation in 18 min. Therefore, mesoporous heterogeneous Ag-WO_3/SBA-15 catalysts can be considered as prospective candidates for AOPs in wastewater treatment.

Also, we successfully synthesized another catalyst Ag/AgBr@m-WO_3 and fully characterized the catalyst. This catalyst shows higher photocatalytic activity on the

degradation of methylparaben using visible light as a source of light. It was observed that the presence of Ag/AgBr on the surface of m-WO_3 brought about a significant enhancement in the photocatalytic performance of Ag/AgBr@m-WO_3 nanocomposite. The enhancement of photocatalytic degradation can be attributed to the SPR due to atomic Ag and consequent enhancement of visible absorption, the reduced of charge recombination due to the formation of metal-semiconductor Schottky junction and the enhancement of surface area due to mesoporosity. Morphological and optical characterizations of the synthesized Ag/AgBr@m-WO_3 were also carried out to explain the efficiency of this photocatalytic material in the process of removal of methylparaben in water.

6.2 Recommendations

Photoctalysis is still in the development step in the development stage various hidden aspects of this technology are yet to be explored in more details. The focus of research in this area is to develop metal oxide photocatalyst as source for degradation of persistent organic pollutants. Unfortunately, at present study WO_3 and modified WO_3 nanocomposite photocatalyst is still not completely mineralization the organic pollutants. Extensive research efforts are needed for the development of new photocatalyst of high activity and complete mineralization of organic pollutant into water and carbon dioxide.

References

1. WHO/UNICEF, Report. Global water supply and sanitation assessment report. *New York Geneva* (2000).

2. Lee, E. J. & Schwab, K. J. Deficiencies in drinking water distribution systems in developing countries. *J. Water Health* **3,** 109–127 (2005).

3. Arai, H., Arai, M. & Sakumoto, A. Exhaustive degradation of humic acid in water by simultaneous application of radiation and ozone. *Water Res.* **20,** 885–891 (1986).

4. Gopal, K., Tripathy, S. S., Bersillon, J. L. & Dubey, S. P. Chlorination byproducts, their toxicodynamics and removal from drinking water. *J. Hazard. Mater.* **140,** 1–6 (2007).

5. Clark, R. M. Predicting Chlorine Residuals in Drinking Water : Second Order Model Predicting Chlorine Residuals in Drinking Water : Second Order Model. **9496,** 152–161 (2015).

6. URANO, K. Empirical rate equation for trihalomethane formation with chlorination of humic substances in water. *Water Res.* **17,** 1797–1802 (1983).

7. Abarnou, A. & Miossec, L. Chlorinated waters discharged to the marine environment chemistry and environmental impact. An overview. *Sci. Total Environ.* **126,** 173–197 (1992).

8. Fujishima, a & Honda, K. Electrochemical photolysis of water at a semiconductor electrode. *Nature* **238,** 37–38 (1972).

9. Hoffmann, M. R., Martin, S. T., Choi, W. & Bahnemannt, D. W. Environmental Applications of Semiconductor Photocatalysis. *Chem. Rev.* **95,** 69–96 (1995).

10. Legrini, O., Oliveros, E. & Braun, A. M. Photochemical processes for water treatment. *Chem. Rev.* **93,** 671–698 (1993).

11. Serpone, N. & Emeline, A. V. Suggested terms and definitions in photocatalysis and radiocatalysis ∗ . **4,** (2002).

12. Miranda, M. A. 2,4,6-Triphenylthiapyrylium cation as homogeneous solar photocatalyst. **129,** 37–42 (2007).

13. Cie, P., Kocot, P., Mytych, P. & Stasicka, Z. Homogeneous photocatalysis by transition metal complexes in the environment. **224,** 17–33 (2004).

14. Hennig, H. Homogeneous photo catalysis by transition metal complexes. **182,** 101–123 (1999).

15. Agrios, A. G. & Pichat, P. State of the art and perspectives on materials and applications of photocatalysis over TiO_2. 655–663 (2005). doi:10.1007/s10800-

005-1627-6

16. Sviridov, D. V. Applied Catalysis B : Environmental Antibacterial activity of thin-film photocatalysts based on metal-modified TiO_2 and TiO_2 : In_2O_3 nanocomposite. **84,** 94–99 (2008).

17. Onoda, K. & Yoshikawa, S. Effect of pre-nitridation treatment on the formation of anatase TiO_2 films by anodization. **34,** 1453–1457 (2008).

18. Falaras, P. & Paraskevi, A. (19) United States (12). (2009).

19. Yang, X. & Wang, Y. Photocatalytic effect on plasmid DNA damage under different UV irradiation time. **43,** 253–257 (2008).

20. Osugi, M. E., Umbuzeiro, G. a, De Castro, F. J. V & Zanoni, M. V. B. Photoelectrocatalytic oxidation of remazol turquoise blue and toxicological assessment of its oxidation products. *J. Hazard. Mater.* **137,** 871–7 (2006).

21. Shchukin, D. G. & Sviridov, D. V. Photocatalytic processes in spatially confined micro- and nanoreactors. *J. Photochem. Photobiol. C Photochem. Rev.* **7,** 23–39 (2006).

22. Fox, M. A. & Dulay, M. T. Heterogeneous Photocatalysis. *Chem. Rev.* **93,** 341–357 (1993).

23. Schäfer, M. *et al.* Systematic study of parameters influencing the action of Rose Bengal with visible light on bacterial cells: comparison between the biological effect and singlet-oxygen production. *Photochem. Photobiol.* **71,** 514–523 (2000).

24. Karunakaran, C. & Dhanalakshmi, R. Phenol degradation on Pr_6O_{11} surface under UV-A light. Synergistic photocatalysis by semiconductors. *Radiat. Phys. Chem.* **78,** 8–12 (2009).

25. Gondal, M. A., Hameed, A. & Yamani, Z. H. Laser induced photocatalytic splitting of water over WO3 catalyst. *Energy Sources* **27,** 1151–1165 (2005).

26. Hameed, a. & Gondal, M. a. Production of hydrogen-rich syngas using p-type NiO catalyst: A laser-based photocatalytic approach. *J. Mol. Catal. A Chem.* **233,** 35–41 (2005).

27. Hameed, A., Gondal, M. A., Yamani, Z. H. & Yahya, A. H. Significance of pH measurements in photocatalytic splitting of water using 355 nm UV laser. *J. Mol. Catal. a-Chemical* **227,** 241–246 (2005).

28. Gondal, M. ., Hameed, A., Yamani, Z. . & Arfaj, A. Photocatalytic transformation of methane into methanol under UV laser irradiation over WO_3, TiO_2 and NiO catalysts. *Chem. Phys. Lett.* **392,** 372–377 (2004).

29. Gondal, M. A., Hameed, A. & Yamani, Z. H. Hydrogen generation by laser transformation of methanol using n-type WO_3 semiconductor catalyst. *J. Mol.*

Catal. A-Chemical **222,** 259–264 (2004).

30. Hameed & Gondal. Laser induced photocatalytic generation of hydrogen and oxygen over NiO and TiO_2. *J. Mol. Catal. A Chem.* **219,** 109–119 (2004).

31. Pirkanniemi, K. Heterogeneous water phase catalysis as an environmental application : a review. **48,** 1047–1060 (2002).

32. Alfano, O. M., Cabrera, I. & Cassano, A. E. Photocatalytic Reactions Involving Hydroxyl Radical Attack I . Reaction Kinetics Formulation with Explicit Photon Absorption Effects. **379,** 370–379 (1997).

33. Ibrahim, U. & Halim, A. Journal of Photochemistry and Photobiology C : Photochemistry Reviews Heterogeneous photocatalytic degradation of organic contaminants over titanium dioxide : A review of fundamentals , progress and problems. **9,** 1–12 (2008).

34. Padmanabhan, P. V. A., Sreekumar, K. P., Thiyagarajan, T. K. & Satpute, R. U. Nano-crystalline titanium dioxide formed by reactive plasma synthesis. **80,** 1252–1255 (2006).

35. Wei, Y., Houten, R. T. Van, Borger, A. R., Eikelboom, D. H. & Fan, Y. Minimization of excess sludge production for biological wastewater treatment. **37,** 4453–4467 (2003).

36. Oller, I., Malato, S. & Sánchez-pérez, J. A. Science of the Total Environment Combination of Advanced Oxidation Processes and biological treatments for wastewater decontamination — A review. *Sci. Total Environ.* **409,** 4141–4166 (2011).

37. Dinnebier, R. E. *Powder Diffraction Theory and Practice Edited by*. (2008).

38. Sing, K. S. Physisorption of Gases by Porous Carbons. *J. Porous Mater.* **2,** 5–8 (1995).

39. Sangwichien, C., Aranovich, G. L. & Donohue, M. D. Density functional theory predictions of adsorption isotherms with hysteresis loops. **206,** 313–320 (2002).

40. Sangwichien, C., Aranovich, G. L. & Donohue, M. D. Density functional theory predictions of adsorption isotherms with hysteresis loops. *Colloids Surfaces A Physicochem. Eng. Asp.* **206,** 313–320 (2002).

41. Wang, Z. L. Transmission Electron Microscopy of Shape-Controlled Nanocrystals and Their Assemblies. *J. Phys. Chem. B* **104,** 1153–1175 (2000).

42. Watts, J. F. & Wolstenholme, J. An Introduction To Surface Analysis By XPS And AES. *J. Chem. Inf. Model.* **53,** 226 (2003).

43. Kubelka, P. & Munk, F. An article on optics of paint layers. *Z. Tech. Phys* **12,** 593–601 (1931).

44. Proudfoot, N. C. Handbook of photographic science and engineering 950-959 (1969).

45. Sacco, O., Vaiano, V., Han, C., Sannino, D. & Dionysiou, D. D. Photocatalytic removal of atrazine using N-doped TiO2 supported on phosphors. *Appl. Catal. B Environ.* **164,** 462–474 (2015).

46. Graymore, M., Stagnitti, F. & Allinson, G. Impacts of atrazine in aquatic ecosystems. *Environ. Int.* **26,** 483–495 (2001).

47. Ta, N., Hong, J., Liu, T. & Sun, C. Degradation of atrazine by microwave-assisted electrodeless discharge mercury lamp in aqueous solution. *J. Hazard. Mater.* **138,** 187–94 (2006).

48. Swan, S. H. *et al.* Semen quality relation to biomarkers of pesticide exposure. *Environ. Health Perspect.* **111,** 1478–1484 (2003).

49. Jiang, H. & Adams, C. Treatability of chloro-s-triazines by conventional drinking water treatment technologies. *Water Res.* **40,** 1657–1667 (2006).

50. Gondal, M. A. *et al.* Visible light photocatalytic degradation of herbicide (Atrazine) using surface plasmon resonance induced in mesoporous Ag-WO_3 /SBA-15 composite. *J. Mol. Catal. A Chem.* **425,** 208–216 (2016).

51. Granados-Oliveros, G., Paez-Mozo, E. A., Ortega, F. M., Ferronato, C. & Chovelon, J. M. Degradation of atrazine using metalloporphyrins supported on TiO2 under visible light irradiation. *Appl. Catal. B Environ.* **89,** 448–454 (2009).

52. Guo, N. *et al.* Uniform TiO_2-SiO_2 hollow nanospheres: Synthesis, characterization and enhanced adsorption-photodegradation of azo dyes and phenol. *Appl. Surf. Sci.* **305,** 562–574 (2014).

53. Zhang, Y., Liu, P. & Wu, H. Development of high efficient visible light-driven N, S-codoped TiO2 nanowires photocatalysts. *Appl. Surf. Sci.* **328,** 335–343 (2015).

54. Zhang, Y., Han, C., Nadagouda, M. N. & Dionysiou, D. D. The fabrication of innovative single crystal N,F-codoped titanium dioxide nanowires with enhanced photocatalytic activity for degradation of atrazine. *Appl. Catal. B Environ.* **168–169,** 550–558 (2015).

55. Malkhasian, A. Y. S. Synthesis and characterization of Pt/$AgVO_3$ nanowires for degradation of atrazine using visible light irradiation. *J. Alloys Compd.* **649,** 394–399 (2015).

56. Santacruz-Chavez, J. A., Oros-Ruiz, S., Prado, B. & Zanella, R. Photocatalytic degradation of atrazine using TiO_2 superficially modified with metallic nanoparticles. *J. Environ. Chem. Eng.* **3,** 3055–3061 (2015).

57. Samsudin, E. M. *et al.* Controlled nitrogen insertion in titanium dioxide for optimal photocatalytic degradation of atrazine. *RSC Adv.* **5,** 44041–44052 (2015).

58. Song, H. *et al.* Synthesis of Fe-doped WO_3 nanostructures with high visible-light-driven photocatalytic activities. *Appl. Catal. B Environ.* **166–167,** 112–120 (2015).

59. Sun, J. hui, Wang, Y. kui, Sun, R. xia & Dong, S. ying. Photodegradation of azo dye Congo Red from aqueous solution by the WO_3-TiO_2/activated carbon (AC) photocatalyst under the UV irradiation. *Mater. Chem. Phys.* **115,** 303–308 (2009).

60. Hayat, K., Gondal, M. A., Khaled, M. M., Yamani, Z. H. & Ahmed, S. Laser induced photocatalytic degradation of hazardous dye (Safranin-O) using self synthesized nanocrystalline WO_3. *J. Hazard. Mater.* **186,** 1226–1233 (2011).

61. Tomer, V. K. & Duhan, S. Highly sensitive and stable relative humidity sensors based on WO3 modified mesoporous silica. *Appl. Phys. Lett.* **106,** (2015).

62. Liu, C. *et al.* Enhanced photocatalytic performance of mesoporous TiO2 coated SBA-15 nanocomposites fabricated through a novel approach: Supercritical deposition aided by liquid-crystal template. *Mater. Res. Bull.* **75,** 25–34 (2016).

63. Zhang, Y., Han, C., Zhang, G., Dionysiou, D. D. & Nadagouda, M. N. PEG-assisted synthesis of crystal TiO_2 nanowires with high specific surface area for enhanced photocatalytic degradation of atrazine. *Chem. Eng. J.* **268,** 170–179 (2015).

64. Xia, F., Ou, E., Wang, L. & Wang, J. Photocatalytic degradation of dyes over cobalt doped mesoporous SBA-15 under sunlight. *Dye. Pigment.* **76,** 76–81 (2008).

65. Hameed, A., Gondal, M. A. & Yamani, Z. H. Effect of transition metal doping on photocatalytic activity of WO_3 for water splitting under laser illumination: Role of 3d-orbitals. *Catal. Commun.* **5,** 715–719 (2004).

66. Zhu, S. *et al.* Synthesis of Cu-doped WO_3 materials with photonic structures for high performance sensors. *J. Mater. Chem.* **20,** 9126 (2010).

67. Sayed Abhudhahir, M. H. & Kandasamy, J. Synthesis and characterization of Manganese doped Tungsten oxide by Microwave irradiation method. *Mater. Sci. Semicond. Process.* **40,** 695–700 (2015).

68. Parthibavarman, D. M. M. & Sangeetha, P. R. M. Influence of Zn doping on structural , optical and photocatalytic activity of WO_3 nanoparticles by a novel microwave irradiation technique. *J. Mater. Sci. Mater. Electron.* **26,** 6823–6830 (2015).

69. Tomer, V. K. *et al.* Humidity-Sensing Properties of Ag^0 Nanoparticles Supported on WO_3-SiO_2 with Super Rapid Response and Excellent Stability. *Eur. J. Inorg. Chem.* **2015,** 5232–5240 (2015).

70. Subash, B., Krishnakumar, B., Swaminathan, M. & Shanthi, M. Enhanced photocatalytic performance of WO_3 loaded Ag-ZnO for Acid Black 1 degradation by UV-A light. *J. Mol. Catal. A Chem.* **366,** 54–63 (2013).

71. Ding, J. *et al.* Selective Deposition of Silver Nanoparticles onto WO3 Nanorods with Different Facets: The Correlation of Facet-Induced Electron Transport Preference and Photocatalytic Activity. *J. Phys. Chem. C* **120,** 4345–4353 (2016).

72. Malik, R. *et al.* Nano gold supported on ordered mesoporous WO3/SBA-15 hybrid nanocomposite for oxidative decolorization of azo dye. *Microporous Mesoporous Mater.* **225,** 245–254 (2016).

73. Luo, B. *et al.* Fabrication of a Ag/Bi_3TaO_7 Plasmonic Photocatalyst with Enhanced Photocatalytic Activity for Degradation of Tetracycline. *ACS Appl. Mater. Interfaces* **7,** 17061–17069 (2015).

74. Linic, S., Christopher, P. & Ingram, D. B. Plasmonic-metal nanostructures for efficient conversion of solar to chemical energy. *Nat. Mater.* **10,** 911–921 (2011).

75. Clavero, C. Plasmon-induced hot-electron generation at nanoparticle/metal-oxide interfaces for photovoltaic and photocatalytic devices. *Nat. Photonics* **8,** 95–103 (2014).

76. Zhang, H., Wang, G., Chen, D., Lv, X. & Li, J. Tuning Photoelectrochemical Performances of Ag - TiO_2 Nanocomposites via Reduction / Oxidation of Ag Ti-C. 6543–6549 (2008).

77. Zhao, D. *et al.* Triblock Copolymer Syntheses of Mesoporous Silica with Periodic 50 to 300 Angstrom Pores Published by : American Association for the Advancement of Science Stable URL : http://www.jstor.org/stable/2894040 REFERENCES Linked references are available on JSTO. **279,** 548–552 (2016).

78. Ma, S., Zhan, S., Jia, Y., Shi, Q. & Zhou, Q. Enhanced disinfection application of Ag-modified g-C_3N_4 composite under visible light. *Appl. Catal. B Environ.* **186,** 77–87 (2016).

79. Kubelka, P. New Contributions to the Optics of Intensely Light-Scattering Materials. Part I. *J. Opt. Soc. Am.* **38,** 448–457 (1948).

80. Vida, G., Josepovits, V. K., Gyor, M. & Deák, P. Characterization of tungsten surfaces by simultaneous work function and secondary electron emission measurements. *Microsc. Microanal.* **9,** 337–342 (2003).

81. Tauc, J. Optical properties and electronic structure of amorphous Ge and Si. *Mater. Res. Bull.* **3,** 37–46 (1968).

82. Wang, D., Tang, J., Zou, Z. & Ye, J. Photophysical and Photocatalytic Properties of a New Series of Visible-Light-Driven Photocatalysts $M_3V_2O_8$ (M = Mg, Ni, Zn). *Chem. Mater.* **17,** 5177–5182 (2005).

83. Sun, S., Wang, W., Zeng, S., Shang, M. & Zhang, L. Preparation of ordered mesoporous Ag/WO_3 and its highly efficient degradation of acetaldehyde under visible-light irradiation. *J. Hazard. Mater.* **178,** 427–433 (2010).

84. Adhikari, R., Gyawali, G., Sekino, T. & Wohn Lee, S. Microwave assisted hydrothermal synthesis of Ag/AgCl/WO_3 photocatalyst and its photocatalytic activity under simulated solar light. *J. Solid State Chem.* **197,** 560–565 (2013).

85. Pan, C. & Zhu, Y. New Type of $BiPO_4$ Oxy-acid salt photocatalyst with high photocatalytic activity on degradation of dye. *Environ. Sci. Technol.* **44,** 5570–5574 (2010).

86. Chen, C. *et al.* Photodegradation of dye pollutants catalyzed by porous $K_3PW_{12}O_{40}$ under visible irradiation. *Environ. Sci. Technol.* **40,** 3965–3970 (2006).

87. Li, G. *et al.* Degradation of Acid Orange 7 using magnetic AgBr under visible light: The roles of oxidizing species. *Chemosphere* **76,** 1185–1191 (2009).

88. Cao, J., Xu, B., Luo, B., Lin, H. & Chen, S. Preparation, characterization and visible-light photocatalytic activity of AgI/AgCl/TiO2. *Appl. Surf. Sci.* **257,** 7083–7089 (2011).

89. Wang, P. *et al.* Highly efficient visible-light plasmonic photocatalyst Ag@AgBr. *Chem. - A Eur. J.* **15,** 1821–1824 (2009).

90. Liu, H., Cao, W., Su, Y., Wang, Y. & Wang, X. Synthesis, characterization and photocatalytic performance of novel visible-light-induced Ag/BiOI. *Appl. Catal. B Environ.* **111–112,** 271–279 (2012).

91. Zang, Y. & Farnood, R. Photocatalytic activity of AgBr/TiO2 in water under simulated sunlight irradiation. *Appl. Catal. B Environ.* **79,** 334–340 (2008).

92. Wang, P. *et al.* Highly efficient visible light plasmonic photocatalyst Ag@Ag(Br,I). *Chem. - A Eur. J.* **16,** 10042–10047 (2010).

93. Chem, J. M., Xiao, M., Jiang, R., Wang, F. & Fang, C. Journal of Materials Chemistry A. 5790–5805 (2013). doi:10.1039/c3ta01450a

94. Wang, P., Huang, B., Dai, Y. & Whangbo, M.-H. Plasmonic photocatalysts: harvesting visible light with noble metal nanoparticles. *Phys. Chem. Chem. Phys.* **14,** 9813–9825 (2012).

95. Zhang, N., Liu, S. & Xu, Y.-J. Recent progress on metal core@semiconductor shell nanocomposites as a promising type of photocatalyst. *Nanoscale* **4,** 2227–38 (2012).

96. Tsung, C. K. *et al.* A general route to diverse mesoporous metal oxide submicrospheres with highly crystalline frameworks. *Angew. Chemie - Int. Ed.* **47,** 8682–8686 (2008).

97. Tang, J., Wu, Y., McFarland, E. W. & Stucky, G. D. Synthesis and Photocatalytic Properties of Highly Crystalline and Ordered Mesoporous TiO_2 Thin Films. *Chem. Commun.* 1670–1671 (2004).

98. Li, L. *et al.* Enhanced photocatalytic properties in well-ordered mesoporous WO_3. *Chem. Commun.* **46,** 7620 (2010).

99. Chen, X. & Mao, S. S. Titanium dioxide nanomaterials: Synthesis, properties, modifications and applications. *Chem. Rev.* **107,** 2891–2959 (2007).

100. Chen, X. *et al.* Enhanced activity of mesoporous Nb_2O_5 for photocatalytic hydrogen production. *Appl. Surf. Sci.* **253,** 8500–8506 (2007).

101. Carp, O., Huisman, C. L. & Reller, A. Photoinduced reactivity of titanium dioxide. *Prog. Solid State Chem.* **32,** 33–177 (2004).

102. Qin, Y., Wang, F., Shen, W. & Hu, M. Mesoporous three-dimensional network of crystalline WO_3 nanowires for gas sensing application. *J. Alloys Compd.* **540,** 21–26 (2012).

103. Teoh, L. G., Hon, Y. M., Shieh, J., Lai, W. H. & Hon, M. H. Sensitivity properties of a novel NO_2 gas sensor based on mesoporous WO_3 thin film. *Sensors Actuators, B Chem.* **96,** 219–225 (2003).

104. Usami, Y., Hongo, T. & Yamazaki, A. Microporous and Mesoporous Materials Phosphate constituent effects on the structure and photocatalytic properties of mesoporous tungsten oxides. *Microporous Mesoporous Mater.* **158,** 13–18 (2012).

105. Yan, X., Zong, X., Qing, G., Lu, M. & Ã, L. W. Progress in Natural Science : Materials International Ordered mesoporous tungsten oxide and titanium oxide composites and their photocatalytic degradation behavior. *Prog. Nat. Sci. Mater. Int.* **22,** 654–660 (2013).

106. Proudfoot, N. C. Handbook of photographic science and engineering.

107. Lin, S., Liu, L., Hu, J., Liang, Y. & Cui, W. Nano Ag@AgBr surface-sensitized Bi2WO6 photocatalyst: Oil-in-water synthesis and enhanced photocatalytic degradation. *Appl. Surf. Sci.* **324,** 20–29 (2015).

108. Yang, Y. *et al.* Fabrication of Z-scheme plasmonic photocatalyst Ag@AgBr/g-C3N4 with enhanced visible-light photocatalytic activity. *J. Hazard. Mater.* **271,** 150–159 (2014).

109. Zhang, J., Li, B. & Yang, W. One-pot synthesis of novel Ag–AgBr@HHSS with superior visible photocatalytic activity. *Microporous Mesoporous Mater.* **194,** 66–71 (2014).

110. Cao, J., Luo, B., Lin, H. & Chen, S. Photocatalytic activity of novel $AgBr/WO_3$ composite photocatalyst under visible light irradiation for methyl orange degradation. *J. Hazard. Mater.* **190,** 700–706 (2011).

111. Wang, P. *et al.* $Ag/AgBr/WO_3$-H_2O: Visible-light photocatalyst for bacteria destruction. *Inorg. Chem.* **48,** 10697–10702 (2009).

112. Zang, Y., Farnood, R. & Currie, J. Photocatalytic activities of AgBr/Y-zeolite in water under visible light irradiation. *Chem. Eng. Sci.* **64,** 2881–2886 (2009).

113. Papadopoulos, C. *et al.* Sonochemical degradation of ethyl paraben in environmental samples: Statistically important parameters determining kinetics, by-products and pathways. *Ultrason. Sonochem.* **31,** 62–70 (2016).

114. Gmurek, M., Bizukoja, M., Mosinger, J. & Ledakowicz, S. Application of photoactive electrospun nanofiber materials with immobilized meso-tetraphenylporphyrin for parabens photodegradation. *Catal. Today* **240,** 160–167 (2015).

115. Terasaki, M., Makino, M. & Tatarazako, N. Acute toxicity of parabens and their chlorinated by-products with Daphnia magna and Vibrio fischeri bioassays. *J. Appl. Toxicol.* **29,** 242–247 (2009).

116. Dobbins, L. L., Usenko, S., Brain, R. A. & Brooks, B. W. Probabilistic ecological hazard assessment of parabens using Daphnia magna and Pimephales promelas. *Environ. Toxicol. Chem.* **28,** 2744–53 (2009).

117. Fatta-Kassinos, D., Bester, K. & Kümmerer, K. *Mass Flows, Environmental Processes, Mitigation and Treatment Strategies 'Xenobiotics in the Urban Water Cycle'. Journal of Chemical Information and Modeling* **53,** (2013).

118. Zhang, Y., Tang, Z. R., Fu, X. & Xu, Y. J. Nanocomposite of Ag-AgBr-TiO_2 as a photoactive and durable catalyst for degradation of volatile organic compounds in the gas phase. *Appl. Catal. B Environ.* **106,** 445–452 (2011).

119. Ye, L. *et al.* Two Different Roles of Metallic Ag on Ag / AgX / BiOX (X = Cl , Br) Visible Light Photocatalysts : Surface Plasmon Resonance and Z- Scheme Bridge. *ACS Cata.* **2,** 1677−1683 (2012).

120. Wang, P. Ag–AgBr/TiO_2/RGO nanocomposite: Synthesis, characterization, photocatalytic activity and aggregation evaluation. *J. Environ. Sci.* 1–12 (2016).

121. Xu, H. *et al.* Preparation, characterization and photocatalytic activity of transition metal-loaded $BiVO_4$. *Mater. Sci. Eng. B Solid-State Mater. Adv. Technol.* **147,** 52–56 (2008).

122. Wang, S. Application of Solid Ash Based Catalysts in Heterogeneous Catalysis. *Environ. Sci. Technol.* **42,** 7055–7063 (2008).

123. Li, H., Zhang, X., Huo, Y. & Zhu, J. Supercritical Preparation of a Highly Active S-Doped TiO_2 Photocatalyst for Methylene Blue Mineralization. *Environ. Sci. Technol.* **41,** 4410–4414 (2007).

124. Zhu, J. *et al.* Colloids and Surfaces A : Physicochemical and Engineering Aspects Fabrication of flower-like Ag @ AgCl/Bi_2WO_6 photocatalyst and its mechanism of photocatalytic degradation. **489,** 275–281 (2016).

125. Zhuang, J. *et al.* Photocatalytic degradation of RhB over TiO_2 bilayer films: Effect of defects and their location. *Langmuir* **26,** 9686–9694 (2010).

126. Jiang, J., Li, H. & Zhang, L. New insight into daylight photocatalysis of AgBr@Ag: Synergistic effect between semiconductor photocatalysis and plasmonic photocatalysis. *Chem. - A Eur. J.* **18,** 6360–6369 (2012).

127. Zhou, Z., Long, M., Cai, W. & Cai, J. Synthesis and photocatalytic performance of the efficient visible light photocatalyst Ag–AgCl/$BiVO_4$. *J. Mol. Catal. A Chem.* **353–354,** 22–28 (2012).

128. An, C., Peng, S. & Sun, Y. Facile synthesis of sunlight-driven AgCl: Ag plasmonic nanophotocatalyst. *Adv. Mater.* **22,** 2570–2574 (2010).

129. Hou, Y., Li, X., Zhao, Q., Quan, X. & Chen, G. TiO_2 nanotube/Ag–AgBr three-component nanojunction for efficient photoconversion. *J. Mater. Chem.* **21,** 18067 (2011).

130. Lin, Y., Ferronato, C., Deng, N., Wu, F. & Chovelon, J.-M. Photocatalytic degradation of methylparaben by TiO_2: Multivariable experimental design and mechanism. *Appl. Catal. B Environ.* **88,** 32–41 (2009).

Vitae

Name : Mohammed Altahir Ibrahim Suliman

Nationality : Sudanese

Date of Birth : 9/24/1989

Email : altahirsdn@gmail.com

Address : Khartoum Bahri, Sudan.

Academic Background : **M.Sc. in Chemistry (May 2017)**

King Fahd University of Petroleum and Minerals

Dhahran, Saudi Arabia

B.Sc in Chemistry (December 2012)

University of Khartoum

Khartoum, Sudan

Research Interests : My research interests are in photocatalysis and Nanostructural materials, and their analytical applications.

Work Experience :

- Teaching assistant Feb. 2017- now

  Chemistry department, KFUPM

- Research assistant Jan. 2016- Jun. 2016

  Centre of Research Excellence in Nanotechnology, (KFUPM)

- Summer Internship Program Jun. 2016- sept. 2016

National University of Singapore, (NUS), Chemistry department

- Full-time Teaching assistant Jan. 2013- Aug. 2014

Department of Chemistry, Faculty of Science, (U of K)

Award and Prize

- Research internship at chemistry department, National University of Singapore, 2016.
- M.Sc. Scholarship, the ministry of higher education, Saudi Arabia, 2014
- University prize for the best academic performance in the final year, University of Khartoum, Sudan 2013.
- Minister of higher education and scientific research prize for the for the best academic performance in the final year, Sudan, 2012.
- Best student of the Arab students exchange program, University of Menoufia, Egypt, 2010

Publications

1. **M. A. Suliman**, M. A. Gondal, M. A. Dastageer, G.-K. Chuah, C. Basheer, "Visible light-induced heterogeneous photocatalytic degradation of methylparaben using Ag/AgBr@m-WO_3" under review in New Journal of Chemistry.

2. M. A. Gondal, **M. A. Suliman**, M. A. Dastageer, G.-K. Chuah, C. Basheer, D. Yang, and A. Suwaiyan, "Visible Light Photocatalytic Degradation of Herbicide (Atrazine) using Surface Plasmon Resonance Induced in Mesoporous Ag-WO_3/SBA-15 Composite," J. Mol. Catal. A Chem., vol. 425, pp. 208–216, 2016.
3. Poster presentation "Synthesis of Visible Light Active Mesoporous Ag-WO_3/SBA-15 Nano Composite Catalyst Based on Surface Plasmon Resonance Enhanced Process" The 4th Saudi International Nanotechnology Conference, Dhahran, Saudi Arabia, October 2016.